Comparative analysis of Binary Black Hole parameters and stellar binaries: a case for primordial black holes

Álvaro Piris Cuiza

Máster en Física Teórica

MÁSTERES DE LA UAM

2019 - 2020

Facultad de Ciencias

UAM Universidad Autónoma de Madrid

Comparative analysis of Binary Black Hole parameters and stellar binaries: a case for primordial black holes

Trabajo de Fin de Máster

Álvaro Piris Cuiza
Supervised by: Prof. García-Bellido Capdevila

Date: December 9, 2020

Instituto de Física Teórica (IFT)
Universidad Autónoma de Madrid

Abstract

We present a review of the computational techniques used for the analysis of strain data from compact binary sources detected by the currently active Advanced LIGO/VIRGO network using a Bayesian inference toolkit (PyCBC Inference) in Python. The parameter space is sampled using dynamically nested sampling and compared to publicly available data available within the Gravitational-Wave Transient Catalogue 1 (GWTC-1). The results are found to be in agreement with this data. Next, correlations in the parameter space present indications that challenge the standard paradigm of BBH formation via the collapse of stars in binary systems. Values of the effective spin averaging across the board to zero may suggest unexpected behaviour either coming from perfectly anti-aligned component spins in equal mass binaries or, alternatively, spinless components. Following up on this, different types of stellar binaries obtained from surveys in the VizieR database are compared to the BBHs in the GWTC-1. Results show that the orbits of some of these have sizes comparable to each other, and that the merge times of stellar binaries would allow sufficient time for them to undergo collapse and form black holes. However, there is an apparent deficit in mass on average that would need to be compensated by the additional processes such as accretion, but which would also induce some spin. In all, this project proposes that stellar black holes should be substituted by other, more favourable candidates, such as primordial black holes, as the main component of these compact systems. The analysis of the Advanced LIGO/VIRGO Run 3 events is necessary in order to provide conclusive results.

Keywords: *Gravitational Waves: Binary Black Hole (BBH), Primordial Black Hole; Stellar Astrophysics: Binaries, Spectroscopic, X-ray; Statistics: Bayesian Inference*

Contents

1 Introduction

Albert Einstein predicted the existence of gravitational waves in 1916, only a year after the formulation of the GR field equations[1]. He concluded that a first order expansion of these would yield plane-wave solutions, waves that would propagate transversely and at the speed of light. These would cause ripples in the fabric of spacetime, albeit extremely small.

The first direct detection of a gravitational-wave signal was made on September 14, 2015, at 09:50:45 UTC[2]. The trigger was detected by both Advanced LIGO detectors located at Hanford (LA) and Livingston (WA) with a time delay of $6.9^{+0.5}_{-0.4}$ms between the former and the latter, which agrees with the 10-ms intersite travel time. This was a phenomenal discov-

ery, and it opened an ample array of opportunities to study these events. Almost five years later, the field is seeing an ever expanding number of possibilities as techniques refine, our available detectors are being upgraded to be more efficient and capable, more are being made operative all over the world and other areas in the frequency space of gravitational waves are being studied. However, even in this golden age, there are still many unknowns about even the more fundamental aspect of the events that have been detected. Two of the most important questions that still need to be formally established involve learning about the specific nature of these orbits, and the processes that drive their characteristics that we can only see from the data.

General relativity has established a fairly complete model which allows to begin the analysis of gravitational wave data with fair simplicity. Since the data needs to be matched to the astrophysical and relativistic models, bayesian inference allows to make statistical estimates of different parameters of the source simply from the strain data from the interferometers. Once these are extracted, they can be specifically analysed in a physical interpretation and conclusions may be drawn. As mysterious as these objects might be, they are still constrained by what is physically possible or not. This allows to provide further insight into them which may be later re-visited once additional data is available.

In this project, we outline the computational techniques that allow bayesian inference to extract numerical values of the parameters. Chapters 2, 3, 4 and 5 provide the background and theoretical foundation on which the project will be built. Chapter 2 contextualises the generation of gravitational waves in a relativistic and astrophysical context, which will be crucial to understand what it is that the detector "detects". Chapter 3 outlines the principles of detection of gravitational waves, including the design of interferometers such as Advanced LIGO and VIRGO, noise sources and matched filtering, which will allow to extract a signal from the data. Chapter 4 provides a brief explanation of the principle behind bayesian inference and the model which will be used to sample the parameter space and obtain the posterior distributions. Finally, Chapter 5 will provide an overview of how this is achieve computationally using a Python toolkit called PyCBC Inference. This section will outline how to provide the inputs and how the data will be handled by the toolkit in order to provide the desired output. In Chapter 6, we review the first results obtained from PyCBC Inference, which estimates the Power Spectral Density of the noise and signal within each detector for each event, allowing to visualise the importance of refining detection techniques in order to reduce noise sources and improve the quality of the data. Chapter 7 provides a comparative analysis of certain pairs sampled parameters in order to obtain correlations that will provide insight into both the nature and the behaviour of the sources. Finally, the project closes in Chapter 8 with a comparative analysis of the orbits of gravitational-wave emitting sources detected by Advanced LIGO/VIRGO detectors with stellar binaries from sky surveys. This allows to probe the stellar collapse model of binary black hole formation and evolution find challenges within this model that need to be addressed.

2 Theory

2.1 GW generation in the astrophysical context

Consider the following gravitational action[3], $\mathcal{S}_G = \mathcal{S}_E + \mathcal{S}_M$, where:

$$\mathcal{S}_E = \frac{c^3}{16\pi G_N}\int \mathrm{d}^4x\sqrt{-g}R \tag{1}$$

is the standard Einstein-Hilbert action and $\mathcal{S}_M$ is the matter action. The Ricci scalar, $R = g^{\mu\nu}R_{\mu\nu}$, is defined from the Ricci tensor, $R_{\mu\nu} = R^{\alpha}_{\mu\alpha\nu}$, which in turn is formally defined from the Riemann tensor, such that:

$$R^{\mu}_{\nu\rho\sigma} = \partial_\rho\Gamma^{\mu}_{\nu\sigma} - \partial_\sigma\Gamma^{\mu}_{\nu\rho} + \Gamma^{\mu}_{\alpha\rho}\Gamma^{\alpha}_{\nu\sigma} - \Gamma^{\mu}_{\alpha\sigma}\Gamma^{\alpha}_{\nu\rho} \tag{2}$$

The energy-momentum tensor, $T^{\mu\nu}$, naturally arises from considering a small variation of $\mathcal{S}_M$, where $g_{\mu\nu} \to g_{\mu\nu} + \delta g_{\mu\nu}$, such that:

$$\delta\mathcal{S}_M = \frac{1}{2c}\int \mathrm{d}^4x\sqrt{-g}T^{\mu\nu}\delta g_{\mu\nu} \tag{3}$$

Therefore, by considering the same perturbation in $\mathcal{S}_E$ and therefore considering a variation in the total action, $\mathcal{S}_G$, one arrives to the Einstein Field Equations (EFEs):

$$R_{\mu\nu} - \frac{1}{2}g_{\mu\nu} = \frac{8\pi G_N}{c^4}T_{\mu\nu} \tag{4}$$

For astrophysical purposes, the local spacetime is normally considered to be flat. When considering gravitational waves, however, one is interested in imbuing this flat spacetime with a weak perturbation such that, to first order, the metric becomes:

$$g_{\mu\nu} = \eta_{\mu\nu} + h_{\mu\nu} \tag{5}$$

where $\eta_{\mu\nu}$ is the standard flat spacetime Minkowski metric and $|h_{\mu\nu}| \ll 1$ is our weak-field perturbation. Since the expansion of the metric is done to first order

in $g_{\mu\nu}$, this theory warrants the name *linearised theory of gravity*. The main objective of the theory will now be to rewrite the EFEs considering this perturbation, and investigate its effects on test particles.

The treatment begins by considering the following assumption: it is always possible to find a coordinate system that satisfies Equation 5. Although seemingly simplistic, this assumption is quite fundamental, as it establishes a preferred reference frame in which the equation holds, thus breaking the invariance of general relativity under coordinate transformation. The breaking of this local invariance is in fact necessary in order to remove nonphysical or unwanted degrees of freedom, but forces the introduction of a residual gauge, such that:

$$x^\mu \to (x')^\mu = x^\mu + \xi^\mu(x) \tag{6}$$

Consequently, the weak-field perturbation transforms as:

$$h_{\mu\nu} \to h'_{\mu\nu}(x') = h_{\mu\nu}(x) - (\partial_\mu \xi_\nu \partial_\nu \xi_\mu) \tag{7}$$

where, in order to maintain the weak-field condition, $|h'_{\mu\nu}| \ll 1$, we require that $|\partial_\mu \xi_\nu|$ be of the same order as $|h_{\mu\nu}|$.

Additionally we can perform global Lorentz transformations on the nearly-flat metric, such that:

$$\begin{aligned} g_{\mu\nu}(x) &\to g'_{\mu\nu}(x') \\ &= \Lambda^\alpha_\mu \Lambda^\beta_\nu g_{\alpha\beta}(x) \\ &= \Lambda^\alpha_\mu \Lambda^\beta_\nu \left(\eta_{\alpha\beta} + h_{\alpha\beta}\right) \\ &= \eta_{\mu\nu} + \Lambda^\alpha_\mu \Lambda^\beta_\nu h_{\alpha\beta} \end{aligned} \tag{8}$$

which allows to define the weak-field transformation $h'_{\mu\nu}(x') = \Lambda^\alpha_\mu \Lambda^\beta_\nu h_{\alpha\beta}(x)$, by which we can conclude that the perturbation $h_{\mu\nu}$ transforms as a Lorentz tensor.

To linear order in $g_{\mu\nu}$, the Riemann tensor takes the form:

$$R_{\alpha\beta\mu\nu} = \frac{1}{2}\left(\partial_\beta \partial_\mu h_{\alpha\nu} - \partial_\alpha \partial\nu h_{\beta\mu} - \partial_\alpha \partial_\mu h_{\beta\nu} - \partial_\beta \partial_\nu h_{\alpha\mu}\right) \tag{9}$$

which is invariant under the gauge transformation described above, making linearised gravity an invariant theory. Additional quantities that are worth defining before going any further include the perturbation trace:

$$h = \eta^{\mu\nu} h_{\mu\nu} \tag{10}$$

and the trace-reversed field perturbation:

$$\bar{h}_{\mu\nu} = h_{\mu\nu} - \frac{1}{2}\eta_{\mu\nu} h \tag{11}$$

The new linear Riemann tensor can be inserted into Equation 4 in order to reformulate the EFEs in terms of the weak-field perturbation:

$$\begin{aligned} &\Box \bar{h}_{\mu\nu} + \eta_{\mu\nu}\partial^\alpha \partial^\beta \bar{h}_{\alpha\beta} - \partial^\alpha \partial_\nu \bar{h}_{\mu\alpha} - \partial^\alpha \partial_\mu \bar{h}_{\nu\alpha} \\ &\quad = -\frac{16\pi G_N}{c^4} T_{\mu\nu} \end{aligned} \tag{12}$$

The tensor $h_{\mu\nu}$ has ten independent components, of which we are only concerned with those that contain physical, dynamically propagating degrees of freedom. To dispose of gauge redundancy, we use the gauge freedom established when the parameter $\xi(x)$ was introduced in order to impose conditions on $h_{\mu\nu}$. The first condition we introduce is known as the *De Donder* (or *harmonic*) gauge[4]:

$$\partial^\mu h_{\mu\nu} = 0 \tag{13}$$

where, as a consequence, $\partial^\mu \bar{h}_{\mu\nu} = 0$. Immediately, this removes the last three terms in Equation 12, reducing it to:

$$\Box \bar{h}_{\mu\nu} = -\frac{16\pi G_N}{c^4} T_{\mu\nu} \tag{14}$$

The introduction of the De Donder gauge automatically removes four degrees of freedom from the weak-field perturbation, leaving $h_{\mu\nu}$ with six independent components. Equation 14 constitutes the most generalised form of the EFEs in linearised gravity theory. Additionally, when considering gravitational waves, a physical phenomena resulting from this theory, one must account for their propagation. When considering this mechanism, we are interested in eliminating as many unnecessary degrees of freedom as possible, and can again make use of gauge freedom to cater to some specifications. The first one is that we require the perturbation to propagate purely spatially, and therefore:

$$h_{00} = h_{0i} = h_{i0} = 0 \tag{15}$$

The second one is that GW propagation must be transverse, which will require that:

$$\partial^\mu h_{\mu\nu} = 0 \tag{16}$$

Finally, we require that the weak-field perturbation be traceless, and therefore $h = 0$. Note that the three conditions defined above are used to describe the propagation of the wave, and are therefore solely defined outside of the source. Putting all of these together, we arrive to a single condition called *transverse-traceless* (or TT) gauge:

$$\Box h_{\mu\nu} = 0 \tag{17}$$

whcih, as before, also leads to $\Box \bar{h}_{\mu\nu} = 0$. With the introduction of the TT gauge, we have effectively reduced the number of degrees of freedom of $h_{\mu\nu}$ to two.

One of the solutions of Equation 17 is that of a plane wave, such that:

$$h_{ij}^{\mathrm{TT}}(z) = \begin{pmatrix} 0 & 0 & 0 & 0 \\ 0 & h_+ & h_\times & 0 \\ 0 & h_\times & h_+ & 0 \\ 0 & 0 & 0 & 0 \end{pmatrix} \cos\left[\omega(t - z/c)\right] \quad (18)$$

provides a full description of the propagation of the wave, and where the parameters h_+ and $h_\times$ describe the two polarisations of the wave.

2.2 Effect on test particles

The motion of a free particle in a spacetime is defined by the geodesic equation:

$$\frac{\mathrm{d}v^\alpha}{\mathrm{d}\tau} + \Gamma^\alpha_{\mu\nu} v^\mu v^\nu = 0 \quad (19)$$

whose initial acceleration if starting at rest would be:

$$\begin{aligned} \left(\frac{\mathrm{d}v^\alpha}{\mathrm{d}\tau}\right)_i &= -\Gamma^\alpha_{00} \\ &= -\frac{1}{2}\eta^{\alpha\beta}\left(\partial_0 h_{\beta 0} + \partial_0 h_{0\beta} - \partial_\beta h_{00}\right) \end{aligned} \quad (20)$$

However, once we consider the condition of purely spatial propagation imposed by the TT gauge, all of the perturbation terms will cancel out, therefore implying that $(\mathrm{d}v^\alpha/\mathrm{d}\tau)_i = 0$. If one considers the naive interpretation of this, one might come to the conclusion that a particle at rest will remain at rest with the passing of a gravitational wave transient. However, one must understand that the consequence of this result is that it is spacetime coordinates of the free particle will remain the same. Because the coordinates are frame-independent, they will "adapt" to the ripples in spacetime, thus seemingly remaining in their fixed positions.

In order to properly study the behaviour of free test particles, it is customary to rather consider the geodesic deviation of a ring of test particles distributed in, for example, the $x - y$ plane and centred at $z = 0$, with a radius ϵ. For a weak gravitational field,

$$\frac{\partial^2 \xi^\alpha}{\partial t^2} = \eta^{\alpha\rho} R_{\rho\mu\nu\sigma} v^\mu v^\nu \xi^\sigma \quad (21)$$

Again, let us consider that these particles are all initially at rest and thus $v^\mu = (1, 0, 0, 0)$. The vector ξ^μ represents the individual distance of the particles to the center of the ring and, since we are considering this precise geometry, it is more useful to work in polar coordinates, such that $x = \epsilon\cos\theta$ and $y = \epsilon\sin\theta$. This makes $\xi^\mu = (0, \epsilon\cos\theta, \epsilon\sin\theta, 0)$ for all particles in the ring and reduces the geodesic deviation equation to:

$$\frac{\partial^2}{\partial t^2}\xi^x = \epsilon\cos\theta\eta^{x\rho}R_{\rho 00x} + \epsilon\sin\theta\eta^{x\rho}R_{\rho 00y} \quad (22a)$$

$$\frac{\partial^2}{\partial t^2}\xi^y = \epsilon\cos\theta\eta^{y\rho}R_{\rho 00x} + \epsilon\sin\theta\eta^{y\rho}R_{\rho 00y} \quad (22b)$$

where the Riemann tensor we are looking to substitute in here is given in Equation 9. Of course, one still needs to consider that the equations must be liable to the action of the transverse-traceless gauge, such that:

$$\frac{\partial^2}{\partial t^2}\xi^x = \frac{\epsilon\cos\theta}{2}\frac{\partial^2}{\partial t^2}h^{(\mathrm{TT})}_{xx} + \frac{\epsilon\sin\theta}{2}\frac{\partial^2}{\partial t^2}h^{(\mathrm{TT})}_{xy} \quad (23a)$$

$$\frac{\partial^2}{\partial t^2}\xi^y = \frac{\epsilon\cos\theta}{2}\frac{\partial^2}{\partial t^2}h^{(\mathrm{TT})}_{xy} + \frac{\epsilon\sin\theta}{2}\frac{\partial^2}{\partial t^2}h^{(\mathrm{TT})}_{xy} \quad (23b)$$

which we can solve to find that:

$$\xi^x = \epsilon\cos\theta + \frac{\epsilon\cos\theta}{2}h_+\cos(\omega t) + \frac{\epsilon\sin\theta}{2}h_\times\cos(\omega t) \quad (24a)$$

$$\xi^y = \epsilon\sin\theta + \frac{\epsilon\cos\theta}{2}h_\times\cos(\omega t) - \frac{\epsilon\sin\theta}{2}h_+\cos(\omega t) \quad (24b)$$

which describes a variation of the distance of the test particles to the centre of the ring relative to a change in the phase when subjected to a transient gravitational wave pulse, apparently unobserved when approaching the problem with the geodesic equation as considered previously.

For the sake of simplicity, let us now consider the situation where we have purely one polarisation orientation (+ or ×). In the case of a purely +-oriented polarisation, the solutions are reduced to:

$$\xi^x = \epsilon\cos\theta\left(1 + \frac{1}{2}h_+\cos(\omega t)\right) \quad (25a)$$

$$\xi^y = \epsilon\sin\theta\left(1 - \frac{1}{2}h_+\cos(\omega t)\right) \quad (25b)$$

On the other hand, in the case where we have a purely ×-oriented polarisation, the equations would become:

$$\xi^x = \epsilon\cos\theta + \frac{\epsilon\sin\theta}{2}h_\times\cos(\omega t) \quad (26a)$$

$$\xi^y = \epsilon\sin\theta + \frac{\epsilon\cos\theta}{2}h_\times\cos(\omega t) \quad (26b)$$

These are represented in Figure 1.

Astrophysical bodies are no strangers to the generation of gravitational waves. It has been well-established that gravitational radiation can be attributed to systems such as pulsars[5], black hole binaries[6], supernovae[7] and even tracing back to the early Universe[8]. In fact, some of these GW-emitting systems may not directly be associated with relativistic phenomena.

The gravitational waveform emitted by a binary system (like a BBH), can be subdivided into three distinct regions according to the dynamics of the systems and the physics involved in describing the channel for gravitational radiation: *inspiral*, *merger* and *ring-down*[9].

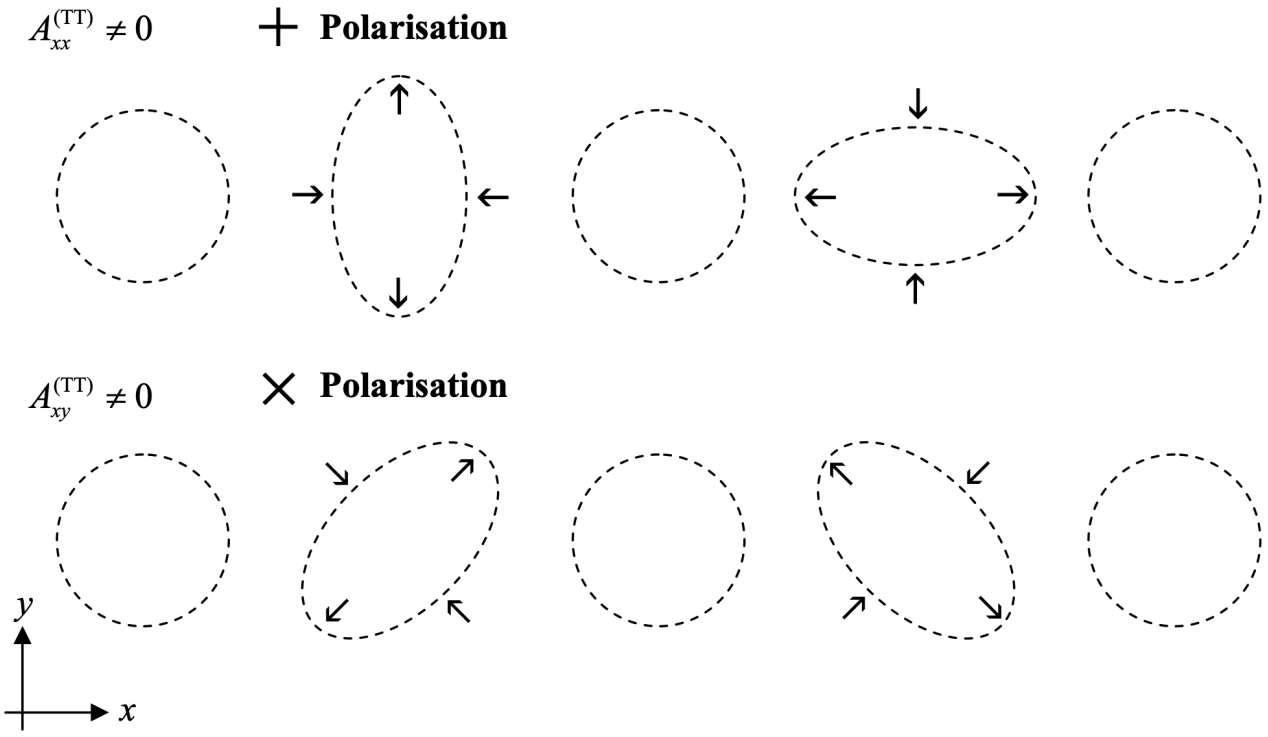

Figure 1: Effect of a gravitational wave transient on a ring of particles. The top row showcases the behaviour in the case of a purely + polarisation, while the second row shows a purely × polarisation.

2.3 Inspiral

Of the three waveform regions, the inspiral has the longest timespan. It is a key part of the waveform, since it encodes many physical parameters of the binary system and sets the maximum amplitude which the signal can reach. It is characterised by a slow ($v \ll c$) Keplerian orbit, where the gravitational radiation generation is done by means of a time varying mass quadrupole moment. This channel can be found in astrophysical systems like binary black holes.

The mass quadrupole is a representation of the mass distribution in a system, and is given by:

$$Q_{ij} = \int \mathrm{d}^3 x \rho(\mathbf{x}) \left(x_i x_j - \frac{1}{3} r^2 \delta_{ij} \right) \tag{27}$$

in a Cartesian coordinate system, with $\rho(\mathbf{x})$ being the mass density distribution[10]. The gravitational-wave strain, h, is expressed in terms of the mass quadrupole moment like:

$$h_{ij} = \frac{2G_N}{c^4} \frac{1}{d_L} \frac{\mathrm{d}^2 Q_{ij}}{\mathrm{d}t^2} \tag{28}$$

where d_L is the luminosity distance to the system.

Astrophysical gravitational-wave emitting systems lose energy and angular momentum as a result of the radiation emission. The rate of energy loss is given by:

$$\begin{aligned} \frac{\mathrm{d}E_{GW}}{\mathrm{d}t} &= \frac{c^3}{16\pi G_N} \int \int |\dot{h}|^2 \mathrm{d}S \\ &= \frac{1}{5} \frac{G_N}{c^5} \sum_{i,j=1}^{3} \frac{\mathrm{d}^3 Q_{ij}}{\mathrm{d}t^3} \frac{\mathrm{d}^3 Q_{ij}}{\mathrm{d}t^3} \end{aligned} \tag{29}$$

In binary systems, this energy loss rate can be averaged to give[11]:

$$\begin{aligned} \frac{\mathrm{d}E_{rad}}{\mathrm{d}t} &= \frac{32}{5} \frac{G^4}{c^5} \frac{\mu^2 M^3}{a^5} F(e) \\ &= \frac{32}{5} \frac{G^4}{c^5} \frac{M_1^2 M_2^1 (M_1 + M_2)}{a^5} F(e) \end{aligned} \tag{30}$$

where $F(e)$ is an eccentricity factor given by:

$$F(e) = \left(1 - e^2\right)^{-7/2} \left(1 + \frac{73}{24} e^2 + \frac{37}{96} e^4 \right) \tag{31}$$

Combining Equations 30 and 31, it becomes clear that highly eccentric binaries are most efficient at radiating gravitational waves. The angular momentum loss rate

is given by:

$$\frac{\mathrm{d}J_{rad}}{\mathrm{d}t} = \frac{32}{5}\frac{G^{7/2}}{c^5}\frac{M_1^2 M_2^2 (M_1+M_2)^{1/2}}{a^{7/2}}\left(1-e^2\right)^{-2}\left(1+\frac{7}{8}e^2\right) \tag{32}$$

As a consequence of this energy and angular momentum loss, binary systems emitting gravitational-wave radiation also experience a separation gradual separation decay, given by[12]:

$$\frac{\mathrm{d}a}{\mathrm{d}t} = -\frac{64}{5}\frac{G^3}{c^5}\frac{M_1 M_2 (M_1+M_2)}{a^4} e\left(1-e^2\right)^{-5/2}\left(1+\frac{121}{304}e^2\right) \tag{33}$$

where M_1 is referred to as the *primary mass* and is conventionally taken as the largest mass component of the binary and $q = M_1/M_2$ is the binary mass ratio (which, by convention is > 1).

2.4 Merger

The Keplerian approximations used in the inspiral become increasingly inaccurate as the binary separation decreases. In the final few orbits before both components merge, general relativistic effects take place and we enter a non-Newtonian regime. Conventionally, the merger phase is initiated once the binary reaches a separation defined as the sum of their *innermost stable circular orbits*[13], a distance given by:

$$a_{ISCO} = \frac{6G_N M}{c^2} \tag{34}$$

or, equivalently, a total of 3 Schwarzschild radii. Here, $M = M_1 + M_2$, is the total mass of the system. Past this separation, a gradual decrease in the orbital radius as seen in the inspiral phase are no longer allowed. Deformations of the black hole horizon of the binary components and tidal forces exerted on each-other and causes the black holes to plunge inwards towards one another[14].

Modelling the dynamics of the BBH binary can no longer be done in the context of a Keplerian basis, instead it is done in the regime of numerical relativity. An analysis of the waveform taking in account the numerical relativity formalism lies outside of the scope of the project and will therefore not be treated further. We recommend the following reviews for a more detailed analysis of numerical relativity ([15, 16]).

2.5 Ringdown

This constitutes the third and last region as well as the most distinct, as it is the only stage of the process where the physics are completely dependant on the properties of the remnant black hole. The violent collapse of the binary components leaves the remnant in an energy level well above its ground level. Due to this instability the remnant BH undergoes pulsation given by spherical harmonics to dispose of the excess.

The signal expected is therefore expected to be given by superimposed quasinormal modes of frequencies characterised by the remnant properties (such as the mass and spin)[17]. Past the ISCO, the binary retains some angular momentum and energy which has not been radiated during the orbital decay, and many of the individual black hole parameters translate into properties of the remnant black hole. For example, we expect that the spin of the final state BH to contain information about the individual spins of the initial binary components and the orbital angular momentum at the ISCO.

3 Gravitational Wave Detection

3.1 Interferometer design

The key to understanding how gravitational-wave signals are processed and the information they contained analysed is to understanding the structure and functionality of gravitational wave detectors. In this section, we provide a small review that will allow us to create a context in which to make a more thorough treatment of data.

Gravitational-wave interferometers can be summarised as kilometre-scale Michelson interferometers[19]. Figure 2 illustrates the general design of one such detector, the Advanced LIGO interferometer[18].

Transient gravitational waves produce small distortions in the space-time metric, which are given by two dimensionless strain polarisations, h_+ and $h_\times$. GW detectors allow to convert this ripples into a measurable signal, by measuring the differential displacement ($\Delta L = \delta L_x - \delta L_y$) of two free-falling test masses (labelled ITM and ETM in Figure 2) along the lengths of the two orthogonal arms ($L_x = L_y = L$) due to the passing of a gravitational wave. This allows to define a relation between this displacement and the arm length, such that $\Delta L = hL$, where h is a linear combination of h_+ and $h_\times$[20]. In practice, these differential displacements manifest as phase shifts in the interference pattern of two identical laser beams travelling along each of the arms and measured at the output.

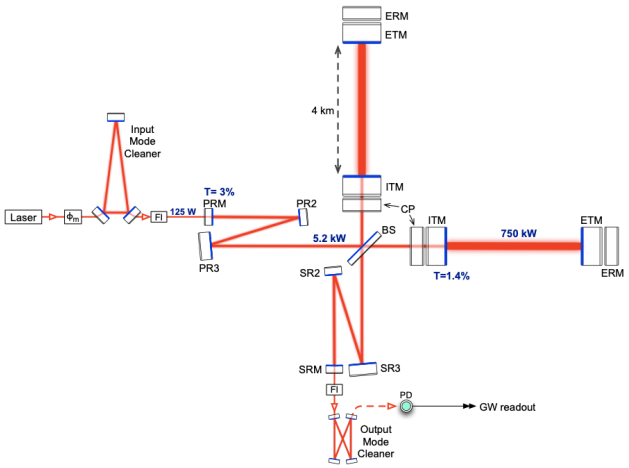

Figure 2: Desing of the Advanced LIGO interferometer. The abbreviations read as follow: ITM (Input Test Mass), ETM (End Test Mass), ERM (End Reaction Mass), CP (Compensation Plate), PRM/PR2/PR3 (Power Recycling Mirrors), BS (Beam Splitter), SRM/SR2/SR3 (Signal Recycling Mirrors), FI (Faraday Isolator), ϕ_m (Phase Modulator), PD (Photodetector) [18].

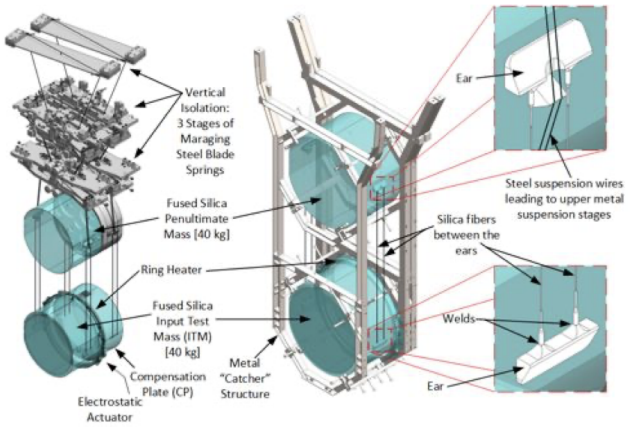

Figure 3: Quadruple pendulum suspension mechanism for the Advanced LIGO test mass [18]

Each component of the detector before the Power-Recycling Mirror (PRM) is designed to fine-tune the input laser beam to match the interferometer mode. The Input Mode Cleaner (IMC) provides positional and modal stability within its three triple-pendulum-suspended mirror cavity, which isolates vibration and significant thermal noise. The Faraday Isolator (FI), is a three-part optical isolator, which removes unwanted interference in the input coming from beam reflections within the interferometer.

With a beam now tuned to the detector's requirements, the laser travels into a 50/50 beam splitter and is divided into two beams, which travel through the perpendicularly-oriented arms. Each arm is equipped with a 4km long Fabry-Pérot optical resonating cavity designed to amplify the phase shift produced by a transient gravitational wave by a factor of 300[21].

The scale of the displacements resulting from the distortions in space-time produced by a transient gravitational wave require the test masses to be, in an ideal situation, completely free from any source of noise (see Section 3.2.1). Both input and end mirrors have a nearly-concentric design for higher stability and power storage, and are made of pure, homogeneous fused silica with a diameter of 34 cm, 20 cm in thickness and a total mass of 40 kg. In order to minimise noise, the test masses are provided with a quadruple pendulum suspension mechanism, which can be seen in Figure 3. Monolithic silica fibres are added between the penultimate and test masses to provide thermal noise isolation.

Power recycling plays a crucial role in the the design of the interferometer, as it amplifies the effective power of the beam going into the Fabry-Pérot resonator. The PRM is a three-mirror resonance cavity slotted between the IMC and the interferometric stage of the detector designed to capture unused light coming from the arms into the beam splitter and effectively sending it back[22]. The PMR receives an input power (coming from the IMC) of up to 125 Watts, as can be seen in Figure 2, and amplifies it such that, within the Fabry-Pérot cavity, the laser reaches powers of around 175 kWatts.

Similarly to the PRM, the Advanced LIGO interferometer utilises a signal recycling cavity (labelled SRM/2/3 in Figure 2) in the final stage to maintain a wide detector frequency response and increasing sensitivity, only transmitting part of the laser beam and sending the rest into the arms again.

The readout of the gravitational wave signal is done by means of an optical filter cavity (called output mode cleaner), tasked with removing higher order spatial modes prior to entering the photodetector, together with DC detection[23].

3.2 Strain sensitivity and noise

3.2.1 Noise sources in gravitational wave detection

As mentioned in Section 3.1, the input and end masses should ideally be free of all sources of noise. In practice, this is not possible and therefore we first need to take account of all possible noise sources.

Figure 4c provides information on the different sources of background noise and their dominant frequency range, which can be classified in different

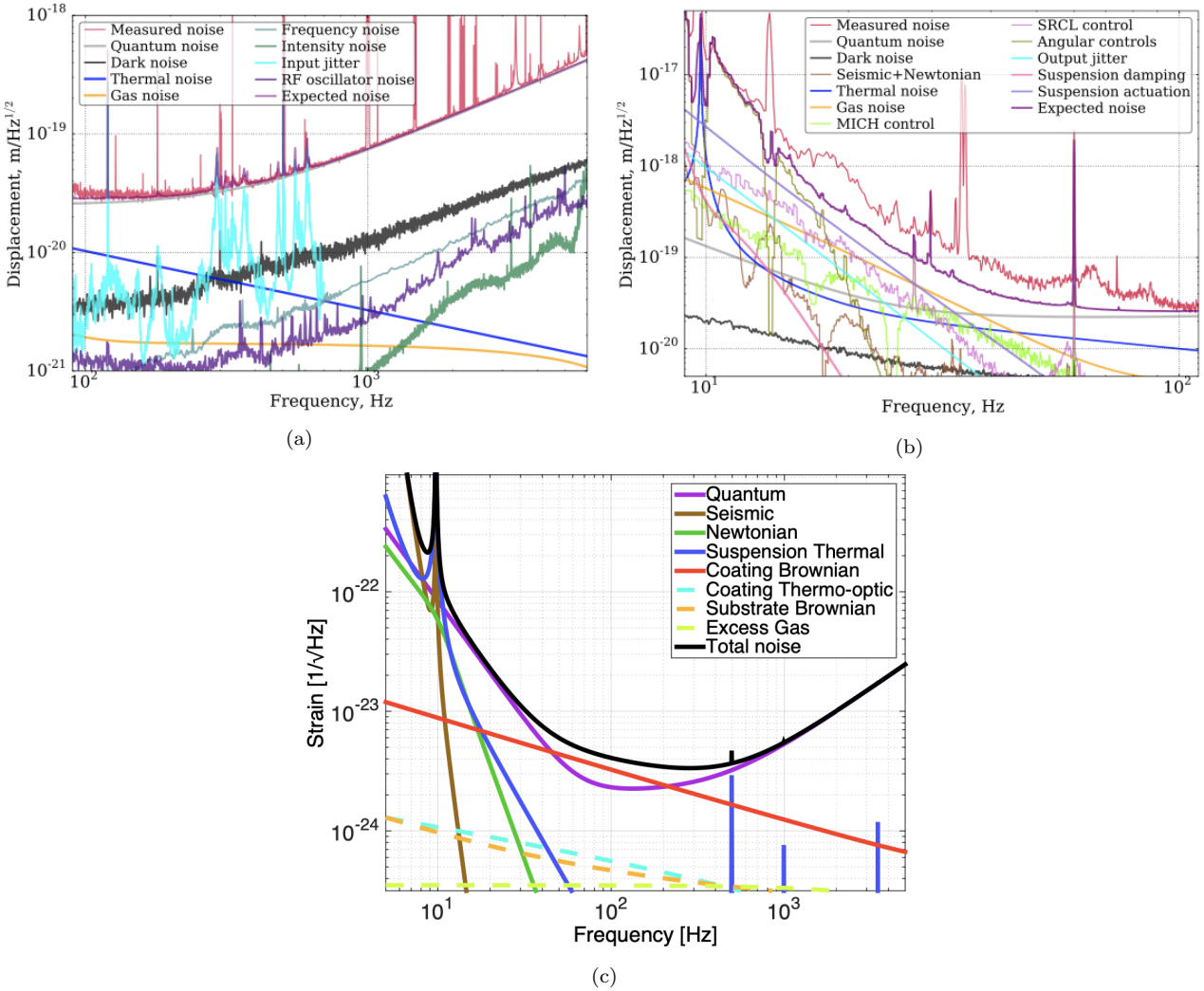

Figure 4: Spectral noise curves associated with the Advance LIGO telescopes. Subfigure (a) and (b) correspond to the noise sources and their curves associated with the Hanford (H1) and Livingston (L1) observatories, respectively. Subfgiure (c) correspond to the design curves associated with general Advanced LIGO observatories.

types[24, 18]:

1. **Quantum noise:** Arises from statistical fluctuations in the photon arrival rate (shot noise) and radiation pressure from photon number fluctuation. This type of noise imposes a limit to the design sensitivity below 40Hz.

2. **Seismic and suspension thermal noise:** Both of these noise sources are significantly dominant under 10Hz. Most of the noise dissipation in the seismic sector is accounted by the quadruple pendulum suspension mechanism described in Figure 3. Suspension thermal noise is due to loss in the silica fibres between the test masses.

3. **Test mass thermal noise:** There are two main types of thermal noise attributed to the test masses. Coating Brownian noise is due to mechanical dissipation of the optical coatings and layers of silica in the test masses, while coating thermo-optic noise is due to thermal dissipation of these. These type of noise are primarily dominant in the 10-500Hz range, but below the overall noise by a factor of 3.

4. **Newtonian gravity noise:** Fluctuating gravitational forces produced by density perturbation in the vicinity of the test masses, mainly due to seismic waves. Above 11Hz, this type of noise is negligible.

5. **Gas noise:** Although the Advanced LIGO/VIRGO components are inside vacuum chambers, residual gas near the optics provides two types of contribution to the noise budget of the detector: (a) thermal motion of the gas molecules exchange momentum with the surface atoms of the mirrors via collisions; (b) forward scattering of photons in the laser beam with gas molecules create modulation in its phase.

3.2.2 Strain sensitivity of Advanced LIGO

Once we understand the noise sources and their impact in the detection potential of gravitational-wave interferometers, the sensitivity curve can be introduced as a necessary and straightforward follow-up. Formally, it quantifies the performance of the detector, by providing a lower bound under which any signal would be indistinguishable, shrouded by interference from thermal, mechanical, optical and quantum noise[24]. Design-wise, we expect the sensitivity curve to be identical to the noise curve, meaning that above it we can expect to have detectable signals. This is an ideal case

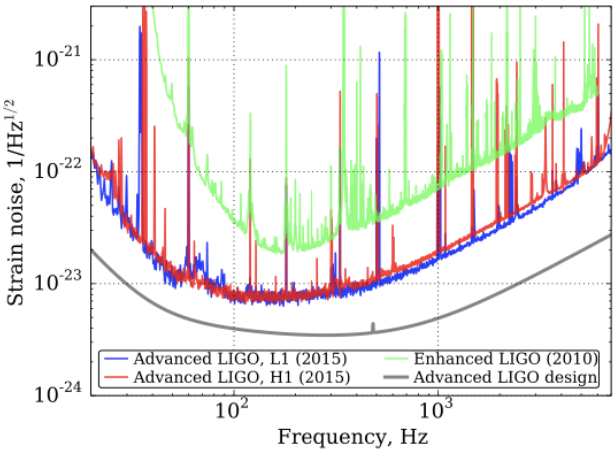

Figure 5: LIGO sensitivity curves.

situation, and we therefore find that the observed sensitivity is generally lower across all frequencies than the expected one (see Figure 5).

3.3 Matched Filtering

The output of the Advanced LIGO detector is given by a time series which contains the differential displacement of the test mass or, alternatively, the phase shift in the interference pattern of the two laser beams after recombining at the output. However, as has been described in the previous section, there must be an account of the noise contributions in the detector, and therefore the output signal can be linearlised, adopting the general form:

$$s(t) = h(t) + n(t) \tag{35}$$

where $h(t)$ is our GW signal, and n(t) encapsulates the noise contribution from all sources.

Matched filtering is a technique which, through the decades, has established itself as the preferred approach to linear signal processing. In general terms, by cross-correlating the interferometer output with a signal corresponding to the expected shape of a GW waveform (called *template*), this method allows us to find "matches" of this signal within the data[25, 26].

Before going into the details of this process, we must first select which part of the gravitational waveform we wish to sample. Performing matched filtering on the early inspiral phase of a compact binary may prove counterproductive. Although the numerical form of the waveform is expected to remain the same for different GW signals, it depends on a wide variety of parameters (masses, spins, orbital eccentricity, etc.), which are unknown for the given detector output. This means that building a template off a given parameter

vector will likely find little correlation within the datastream provided by the interferometer, due to the large difference in parameter vectors[27]). Instead, we chose to perform matched filtering closer to the merger phase of the compact binary, where the features become more distinctive for each event.

To perform matched, we introduce the Signal-to-Noise Ratio (SNR) as an indicator of the level at which the template is present within the signal. For a given template, $h(t)$, and strain datastream, $s(t)$, the SNR, $\rho(t)$, is given by[28]:

$$\rho^2(t) \equiv \frac{1}{\langle h|h\rangle}|\langle s|h\rangle(t)|^2 = \frac{\langle s|h_+\rangle^2 + \langle s|h_\times\rangle^2}{\langle h|h\rangle} \tag{36}$$

where the inner product $\langle s|h\rangle$ is given by:

$$\langle s|h\rangle(t) = 4\mathfrak{Re}\left[\int_0^\infty \frac{\tilde{s}(f)\tilde{h}^*(f)}{S_n(f)} e^{-2\pi i f t}\mathrm{d}f\right] \tag{37}$$

Equivalently,

$$\langle h|h\rangle(t) = 4\mathfrak{Re}\left[\int_0^\infty \frac{\tilde{h}(f)\tilde{h}^*(f)}{S_n(f)}\mathrm{d}f\right] \tag{38}$$

where any quantity $\tilde{a}(f)$ is the Fourrier transform of the same time domain quantity:

$$\tilde{a}(f) = \int_{-\infty}^{\infty} a(t) e^{-2\pi i t f}\mathrm{d}t \tag{39}$$

and $S_n(f)$ is the Power Spectral Density (PSD) of the detector noise, defined by:

$$\langle \tilde{s}(f)\tilde{s}(f')\rangle = \frac{1}{2} S_n(f)\delta(f - f') \tag{40}$$

At this point, we make a small pause to note two small but relatively important details. First, the convolutions $\langle s|h\rangle$ and $\langle h|h\rangle$ (Equations 37 and 38) is done by integrating over the entire frequency range, $[0, \infty)$. This is not practically useful, and we instead decide to impose a highpass (f_{high}) and lowpass (f_{low}) frequency filter in a process called *bandpassing*, allowing the rewrite these equation as:

$$\langle s|h\rangle(t) = 4\mathfrak{Re}\left[\int_{f_{low}}^{f_{high}} \frac{\tilde{s}(f)\tilde{h}^*(f)}{S_n(f)} e^{-2\pi i f t}\mathrm{d}f\right] \tag{41}$$

$$\langle h|h\rangle(t) = 4\mathfrak{Re}\left[\int_{f_{low}}^{f_{high}} \frac{\tilde{h}(f)\tilde{h}^*(f)}{S_n(f)}\mathrm{d}f\right] \tag{42}$$

Secondly, note that in the presence of a stationary, purely Gaussian noise source, Equation 42, reduces to 2, which greatly simplifies calculations and, furthermore, allows for the SNR to be the only detection statistic to be considered. The reality is, however, that although the noise contribution of thermal, quantum and seismic sources can be taken to be so, there exist an important non-stationary, non-Gaussian transient noise component, composed mainly of instrumental and environmental sources[29], outlined in Section 3.2.1.

Transient noise mitigation is achieved by introducing the chi-squared method as an additional statistical test, determining whether the time-frequency distribution of the data coincides with the expected one from the template. The process involves dividing the template into frequency bins and calculating the SNR corresponding to each individual bin. Then, the $\chi 2$ value is given by:

$$\chi^2 = p\frac{1}{\langle h|h\rangle}\sum_{i=1}^{p}\left|\langle s|h_i\rangle - \frac{\langle s|h\rangle}{p}\right|^2 \tag{43}$$

where p corresponds to the number of frequency bins. The bin number can be tailored to the inherent parameters of template the analysis is being performed on. There is a physical significance in this, as lower-mass binaries (for example, binary neutron stars) generate longer waveforms and their signals therefore contain more cycles pre-merger. In cases like these, we are interested in increasing the number of bins, making the test more accurate. Higher values of χ^2 are indicators of noise transient likelihood, instead of signal. We normalise it such that, for signals, this value should approach unity, introducing the reduced chi-squared:

$$\chi_r^2 = \frac{\chi^2}{2p - 2} \tag{44}$$

To further suppress triggers from noise transients, the matched SNR (given by Equation 36) is re-weighted such that:

$$\hat{\rho} = \begin{cases} \rho/\left[(1 + (\chi_r^2)^3)/2\right]^{1/6}, & \chi_r^2 > 1 \\ \rho, & \chi_r^2 \leq 1 \end{cases} \tag{45}$$

This re-weighted SNR allows us to clearly define limit for signal acceptance, such that any trigger with $\hat{\rho} < 5$ is conventionally discarded.

4 Statistical method

4.1 Review of Bayesian inference

At the heart of Bayesian inference processes lies an aim to extract numerical information that is being encoded into a dataset, making it not obvious with a simple an analysis of the data. It does so by considering a model (or hypothesis, $\mathcal{H}$) which the data is expected to follow; this model is composed by a vector of parameters ($\vec{\theta}$) which can be one dimensional

or multi-dimensional, which will later influence the way in which such information is visualised. At the very least, Bayesian inference seeks to provide an estimate of which numerical values of each parameter are most probable. Therefore, the primary objective of this method is to construct and populate a *posterior distribution* ($p(\vec{\theta}|d,\mathcal{H})$), which is a Probability Density Function (PDF) of a parameter vector ($\vec{\theta}$) with respect to a dataset (d).

The posterior distribution is formally defined using the *Bayes' theorem*, which states that:

$$p(\vec{\theta}|d,\mathcal{H}) = \frac{p(d|\vec{\theta},\mathcal{H})p(\vec{\theta},\mathcal{H})}{p(d,\mathcal{H})} \tag{46}$$

where $p(d|\vec{\theta},\mathcal{H})$ is called *likelihood*, $p(\vec{\theta},\mathcal{H})$ is the *prior distribution* and $p(d,\mathcal{H})$ is a normalisation constant referred to as *marginalised likelihood* or *evidence*:

$$p(d,\mathcal{H}) = \int \mathrm{d}\vec{\theta}\; p(\vec{\theta},\mathcal{H})p(d|\vec{\theta},\mathcal{H}) \tag{47}$$

The prior distribution establishes our knowledge of the parameters we wish to infer, and is therefore a probability distribution of the parameter space, chosen before any consideration of the data to analyse. Common priors to use are *uniform*, where the normalised expression is given by:

$$p(\theta_i,\mathcal{H}) = \begin{cases} 1/(\theta_{i,max}-\theta_{i,min}), & \theta_{i,min} \le \theta \le \theta_{i,max} \\ 0, & \text{otherwise} \end{cases} \tag{48}$$

where $\theta_{i,min}$ and $\theta_{i,max}$ limit the values of the parameter θ_i is allowed to take. Other priors, like *gaussian*, are also possible to and, in some cases, superior to uniforms, but where the latter creates a clear bias to a specific subset of values (informed prior), the former establishes a very unbiased approach to the inference of the parameter at hand (uninformed prior).

Simply put, the likelihood defines the model on which we wish to extract the data. Formally, it is constructed by demanding that the residual signal formed by subtracting the observed signal to the waveform model $\mathbf{r} = \mathbf{s} - \mathbf{R}^*\mathbf{h}$, where $\mathbf{s}$ is the datastream coming from the detector, $\mathbf{h}$ is the two gravitational-wave polarisations and $\mathbf{R}$ is a time-delay operator which describes the detector's response to a signal; be consistent with the model for the noise, $\mathbf{n}$[30]. The choice of model depends on the user and the inference tool used for this project (PyCBC Inference, see Section 5) offers a variety of them to work with. This project, and the strain data analysis, uses the Marginalised Phase Likelihood model (see Section 4.2).

In the context of BBH systems, the signal received at the detector is described by a 15-dimensional parameter space: ($M_{d,1}$, $M_{d,2}$, χ_1, χ_2, $\chi_{\theta,1}$, $\chi_{\theta,2}$, $\chi_{\phi,1}$, $\chi_{\phi,2}$, α, δ, d_L, t_c, Φ, ι, ψ), where M_1 and M_2 are the masses of the components (may be substituted by the mass ratio, $q = M_1/M_2$, and the chirp mass, $\mathcal{M}$, defined in the *detector frame*, where special emphasis is put on this for reasons that will become apparent later on, chi_i, $chi_{\theta,i}$ and $\chi_{\phi,i}$ are the spin parameters in polar coordinates (may be replaced by Cartesian coordinates, $\chi_{x,i}$, $\chi_{y,i}$ and $\chi_{z,i}$), α and δ are the right ascension and declination of the source, respectively, d_L is the luminosity distance to the source, t_c is the arrival time of the signal, Φ is a coalescence phase and ψ is a polarisation angle[31].

Ideally, we wish to extract values for all of the above parameters from the strain data, and therefore the Bayesian analysis will be complex and involve many priors.

4.2 Marginalised Phase Likelihood model

The PyCBC Inference package (see Section 5) provides many statistical models to work with, but for this particular project we use where we assume a stationary Gaussian noise and where the signal is marginalised of the coalescence phase, Φ. For this method, we assume that the signal can be modelled as:

$$\tilde{h}(f;\Theta,\Phi) = A(f;\Theta)e^{i\Psi(f;\Theta)+i\Phi} \tag{49}$$

where $h(\tilde{f})$ is the Fourrier transform of the strain time-series, Θ is the parameter space and Φ is the phase constant to marginalise over. Assuming a stationary and Gaussian noise, the posterior is given by:

$$p(\Theta,\Phi|d) \propto p(\Theta)p(\Phi)p(d|\Theta,\phi) \propto \frac{p(\theta)}{2\pi} \times \exp\left[-\frac{1}{2}\sum_i^{N_D}\langle h_i(\Theta,\Phi)-d_i, h_i(\Theta,\Phi)-d_i\rangle\right] \tag{50}$$

where we have assumed a prior $p(\Theta)$, N_D is the number of detectors and h_i and d_i are the model and signal obtained for detector i. For this model, we assume a uniform prior on $\Phi \in [0, 2\pi)$. The inner product (defined in Equation 38) in the exponent can be expanded as:

$$-\frac{1}{2}\langle h_i-d_i, h_i-d_i\rangle = \langle h_i, d_i\rangle - \frac{1}{2}\langle h_i, h_i\rangle - \frac{1}{2}\langle d_i, d_i\rangle \tag{51}$$

which we can solve to find:

$$-\frac{1}{2}\langle h_i-d_i, h_i-d_i\rangle = \Re\{O(h_i^0, d_i)e^{-i\Phi}\} - \frac{1}{2}\langle h_i^0, h_i^0\rangle - \frac{1}{2}\langle d_i, d_i\rangle \tag{52}$$

where $h_i^0 \equiv \tilde{h}_i(f;\Theta,\Phi=0)$ and:

$$O(h_i^0,d_i) \equiv 4\int_0^\infty \frac{h_i^{0,*}(f)\tilde{d}_i(f)}{S_n(f)}\mathrm{d}f \tag{53}$$

From a practical standpoint, bandpassing (see Section 3.3) will be necessary when this computation is carried out. We can now gather all explicitly phase-independant terms into a single function:

$$\alpha(\Theta,d) \equiv \exp\left[-\frac{1}{2}\sum_i \langle h_i^0,h_i^0\rangle + \langle d_i,d_i\rangle\right]. \tag{54}$$

Finally, we can marginalise over the phase by integrating:

$$\begin{aligned} p(\Theta|d) &\propto p(\Theta)\alpha(\Theta,d)\frac{1}{2\pi} \\ &\times \int_0^{2\pi}\exp\left[\Re\left\{e^{-i\Phi}\sum_i O(h_i^0,d_i)\right\}\right]\mathrm{d}\Phi = p(\Theta)\alpha(\Theta,d)\frac{1}{2\pi} \\ &\times \int_0^{2\pi}\exp\left[x(\Theta,d)\cos(\Phi)+y(\Theta,d)\sin(\Phi)\right]\mathrm{d}\Phi \end{aligned} \tag{55}$$

where the solution to the last integral is given by $2\pi\mathcal{I}_0\left(\sqrt{x^2+y^2}\right)$, where $\mathcal{I}_0$ is the modified Bessel function of the first kind. Logging the marginalised posterior, we arrive to:

$$\begin{aligned} \log p(\Theta|d) \propto \log p(\Theta) + \mathcal{I}_0\left(\left|\sum_i O(h_i^0,d_i)\right|\right) - \\ \frac{1}{2}\sum_i\left[\langle h_i^0,h_i^0\rangle - \langle d_i,d_i\rangle\right] \end{aligned} \tag{56}$$

5 Parameter Extraction: the PyCBC Inference package

PyCBC Inference package is a set of Python modules part of the open source PyCBC toolkit, which allows to implement Bayesian analysis on gravitational wave data. The main input in PyCBC Inference is a series of configuration files which can contain different sections.

5.1 The Prior configuration file

The first file, [priors.ini], is formed of many sections that describe the priors of all of the relevant sampling parameters. The first section, [model], described the method with which the likelihood will be calculated (in this case, we are used the [marginalized_phase] model), and a [low-frequency-cutoff], which limits the accepted frequencies to above 20 Hz. The [variable_params] sections simply seeks to explicitly initialise the parameters we are interested in obtaining posteriors to. PyCBC inference offers a wide array of variables to sample; however, if one is interested in making estimates on one that is not provided, the [waveforms_transforms-param] section allows to define new parameters based on pre-existing [variable_params]. Some parameters are which actively participate in the estimation process but which do not necessarily change themselves can be defined in the [static_params] section. In here, we find variables like [approximant], which defines the numerical relativity approach to processing a gravitational wave waveform (in this project [IMRPhenomPv2]), the lower frequency bound ([f_lower]) and a reference frequency ([f_ref]), and the [trigger_time] for the event (imported from a different file, see below). The rest of the sections in this file are dedicated to defining the priors of the [variable_params]. The general form of each is fairly similar, and requires defining a type of prior to use and some upper and lower boundaries of accepted values for the variable. Ideally, we want to use as uninformed priors as possible and therefore the majority of our distributions are conventionally uniform ([uniform], [uniform_angle] and [uniform_sky]) with respect to the specific parameter. However, one can set [gaussian] and even [arbitrary] distributions, as well as importing them from a file ([fromfile]). In fact, informed priors will play a crucial role in this very project as we will see later.

5.2 The Sampler configuration file

The [sampler.ini] file defines the [sampler] used in order to perform the parameters estimation procedure. PyCBC Inference provides several sampling methods including MCMC ([emcee]), parallel-tempered MCMC ([emcee_pt]) and several types of nested sampling. For this project, dynamically nested sampling ([dynesty][32]) was found to be the most efficient in terms of convergence time. Dynamically nested sampling is a extension of nested sampling in which samples are adaptively drawn during a run in order to chose better areas in the parameter space that will maximise a chosen function. In other words, it allows nested sampling to adapt and evolve in real time with the posterior, improving both accuracy and efficiency. This sampling method seeks to make an estimate of the evidence ($\mathcal{Z}$) by assuming that the integral of the posterior over all sampling parameters is equivalent to a volume integral of the prior[33]:

$$X(\lambda) \equiv \int_{\Theta:\mathcal{L}(\Theta)>\lambda}\pi(\Theta)\mathrm{d}\Theta \tag{57}$$

Contained within an iso-likelihood contour set by

$\mathcal{L}(\Theta) = \lambda$ via:

$$\mathcal{Z} = \int_0^{+\infty} X(\lambda)\mathrm{d}\lambda = \int_0^1 \mathcal{L}(X)\mathrm{d}X \tag{58}$$

assuming that $\mathcal{L}(X(\lambda)) = \lambda$ exists. Once the iso-likelihood contour $\mathcal{L}_i \equiv \mathcal{L}(X_i)$ associated with a bunch of samples is found from the poor volume $1 > X_0 > X_1 > ... > X_N > 0$ the evidence can be computed using standard integration techniques such as the trapezoid rule.

This is done by first drawing a K number of "live points" ([nlive]) from the prior $\pi(\Theta)$. At each iteration, i, the point with the lowest likelihood is removed and replaced with a new live point sampled from the prior such that $\mathcal{L}_{i+1} \geq \mathcal{L}_i$.The prior volume of the removed live point (now called a dead point), is given by:

$$\ln X_i \approx -\frac{i \pm \sqrt{i}}{K} \tag{59}$$

The evidence can then be numerically estimated from a set of N dead points via

$$\mathcal{Z} = \int_0^1 \mathcal{L}(X)\mathrm{d}X \approx \hat{\mathcal{Z}} = \sum_{i=1}^{N} f(\mathcal{L}_i) f(\Delta X_i) \equiv \sum_{i=1}^{N} \hat{w}_i \tag{60}$$

where $\hat{w}_i$ is the dead point's estimated weight. The same set of dead points allows to estimate the posterior, such that:

$$P(\Theta_i) = P(X_i) \equiv p_i \approx \hat{p}_i = \frac{\hat{w}_i}{\sum_{i=1}^{N} \hat{w}_i} = \frac{\hat{w}_i}{\hat{\mathcal{Z}}} \tag{61}$$

The process repeats until some stopping criteria is met. This is done by considering that that remaining evidence at each iteration can be bounded by:

$$\Delta\hat{\mathcal{Z}}_i \approx \mathcal{L}_{\max} X_i \tag{62}$$

where $\mathcal{L}_{\max}$ is the maximum likelihood contained within the set of K live points. Therefore, one can construct a stopping criterion such that:

$$\Delta \ln \hat{\mathcal{Z}}_i \equiv \ln\left(\hat{\mathcal{Z}}_i + \Delta\hat{\mathcal{Z}}_i\right) - \ln \hat{\mathcal{Z}}_i \tag{63}$$

where the sampling of new live points will stop at a given $\Delta \ln \hat{\mathcal{Z}}_i$ ([dlogz]).

5.3 The Data configuration file

The [data.ini] file contains a single section, [data], which contains all of the remaining information required to perform the analysis. Within this file, explicit information about the interferometers being used must be provided, achieved in the [instruments] variable to initialise them and then by providing the [channel-name], which will retrieve all information on that detector relevant to the analysis at hand. This is particularly important for, say, sky localisation, as being able to match the exact location of the interferometer to its corresponding signal is necessary in order to make estimates on the source's position. The variable [frame-files] provides the location within the computer of the strain timeseries pertaining to the specific detector and event that is being studied, which are downloaded from the GW Open Science Centre[34] as .gwf files. These have been down-sampled from 16 kHz to 4kHz for less computational strain, and contain a total of 4096 seconds of strain data (which will later need to be trimmed). To do so, the [trigger-time] variable is set in order to set a reference point around which the data will be analysed. It aims to be long enough so that a significantly large portion of the waveform is included while still being admitted by the prior. This is achieved by introducing the [analysis-start-time] variable, which provides a 6 second window before the trigger time to allow for a signal to enter the resolvable frequency range of Advanced LIGO/VIRGO detectors. Considering that the waveform duration is largely dependant on the mass of the source, where less massive systems have a longer waveform, a six second window behind the trigger time correspond to a total mass of approximately 20 $M_\odot$, which corresponds to the lowest total mass resolvable by the prior, thus including all possible detectable masses in the analysis. Another margin of 2 second is set after the trigger time by the [analysis-end-time] to provide ample time after the trigger for the merger and ringdown to take place.

This configuration file also includes all of the information necessary to estimate the Power Spectral Density (PSD) of the detector noise, which is crucial for techniques such as matched filtering and bayesian inference. The program does this independently, but requires a set of parameters. The [psd-estiamation] variable describes the the method used for this estimation, which in our case is Welch-line ([median-mean]), with a window of 512 seconds ([psd-end-time] - [psd-start-time]). The entire period is divided into 8 second-long segments ([psd-segment-length]) with an overlapping of 4 seconds on each side ([psd-segment-stride]). In order to limit the corruption the the analysis due to the convolution of the inverse PSD with the data at the beginning and end of the analysis, 4 seconds are substracted/added at the start/end times. This won't affect the end results, as the analysis waveform is entirely contained within the boundaries that were set previously ($t_{c,-6s}^{+2s}$). The final parameters are used to complete the analysis at hand, including the [sample-

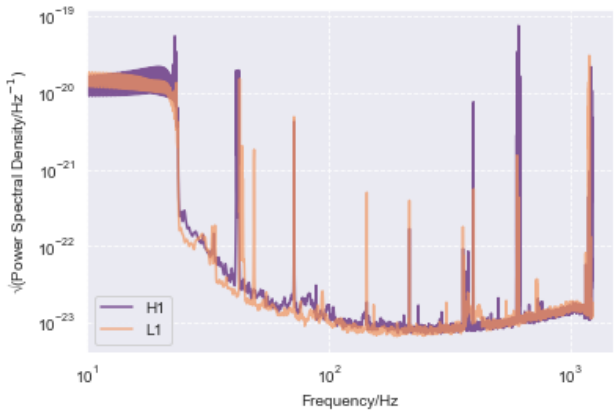

Figure 6: Power spectral density in the Advanced LIGO interferometers (H1, L1) and VIRGO (V1) as computed by PyCBC from the strain data from event GW150914.

rate], which ensures that the data is resampled with a frequency of 2048 Hz. The data is also padded with 8 seconds at the start and end of both the analysis and PSD times ([pad-data]), which is to be discarded as soon as the highpass filter is applied ([strain-high-pass]). For this project, a filter of 15 Hz was applied, well below the frequency cutoff for the likelihood integral. This is done so as to minimise numerical errors from large amplitude, low frequency noise sources.

6 Power Spectral Density

As explained in Section 5.3, PyCBC Inference takes care of estimating the noise PSD for each detector, which is necessary in order to construct the logarithmic posterior and computing the SNR. After running the sampler, the results are outputted to an HDF5 file, part of which stores the PSD for each of the detectors used.

Figure 6 showcases the different PSDs estimated for each detector using the open-source GWF files belonging to the first detected gravitational-wave event, GW150914. This event is characterised by a combined SNR of 24 amongst the detectors that produced a trigger (H1 and L1).[2] The curves presented in the figure are crucial to determine at which "stage" (or frequency) the signal will enter the detectable capabilities of the respective detector. As we can see, the "expected" window of detectability begins at approximately 20 Hz, past a sudden drop in the PSD. After that, the general shape of the curve is defined by the different noise contributions (Gaussian and stationary in this case) that arise with the detector chamber, which depend on the specifics of the interferometer design, hence the slightly different curves for each site. The study of these curves is extremely important, because each gravitational wave source inhabits its own detectability region in the frequency domain. Binary black holes are fortunately located within the frequency window represented in the figure. If, however, we were to consider other types of sources such as Supermassive Black Holes Binaries (SMBHB), located in the nanohertz to microhertz range[35, 36], or Extreme Mass Ratio Inspirals (EMRI), in the milli-hertz range[37, 38], the signal would be completely overshadowed by the detector noise. Therefore, a comprehensive understanding of the PSD curves allows for insight into the limitations of the detector, and therefore allows to provide alternative designs to study other GW sources, for example, space-based interferometers[39] or Pulsar Timing Arrays[40].

This is best seen by superimposing to the PSD the strain as read in the frequency domain, called STILDE. Figure 7 showcases this for the GW150914 event for each detector. As can be seen, the signal is consistently prevalent over the noise in the range of $20 - 10^3$Hz which allows to conclude that searches for the coalescence of compact binary inspirals is well-found in ground-based interferometers such as the Advanced LIGO/VIRGO sites. To further increase sensitivity and accuracy, searches into how to further reduce the noise contributions are necessary or, alternatively, the introduction of more detectors, such as KAGRA[41], LIGO India[42] and the Einstein Telescope[43].

7 Analysis of GWTC-1 samples

Most importantly, the [results.hdf] file contains the entire sample set for the desired parameters. These samples allow to make statistical estimates of the physical properties of the source, which will consequently be used to inquire about the consistency of the current BBH and gravitational wave models. Once the parameter extraction procedure is complete, the aim is to investigate the correlation between such properties, thus providing insightful information about the physics behind these sources and the model itself.

At first glance, however, we have no way of making sure that the sampler used is providing an accurate estimate of the source properties other than observing that the result of the sampler obviously converges to some reasonable value. In order to test the validity of the numerical estimates, we can perform a comparative analysis using the samples provided in the Gravitational Wave Transient Catalog 1[44, 45], referred to in this project as GWTC-1. The data contained within this catalog provides a useful reference that will serve as the base on which we measure the accuracy of the sampler.

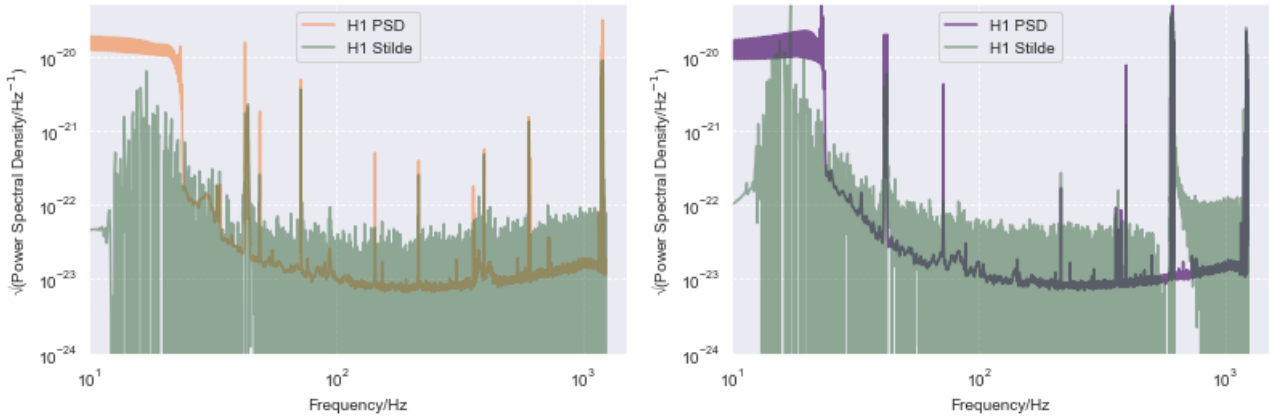

(a) (b)

Figure 7: Signal strain (stilde) and noise PSD (PSD) contained in each detector for the event GW170814 as computed by PyCBC Inference. Subfigure (a), (b) and (c) corresponds to the Hanford (H1), Livingston (L1) and VIRGO (V1) interferometers, respectively. The signal created from the data is composed of a waveform that spans frequencies from approximately 20Hz to about 1.5×10^3Hz, most of which enter within the detectable range of the Advanced LIGO/VIRGO detectors, with exception of some very narrow windows where the sensitivity curve encounters a peak due most probably to some source of noise.

Figure 8 showcases the results of the sample file from both the PyCBC Inference analysis and obtained directly from the GWTC-1 repository. The results show a clear agreement between both datasets, albeit the convergence is more pronounced in the GWTC-1 samples. However, we are not looking for either a direct match of the data or to improve the level of accuracy currently available to the public, but rather a confirmation that the values the sampler is converging to are correct. Table 1 contains all of the numerical data of the sample files for all events.

The large number of variable parameters being studied in this project, namely the existence of subsets of variables which cannot really be compared between each other from an intuitively physical standpoint, will warrant separate studies of groups of sampled variables in order to draw conclusions that provide insight into properties of the gravitational-wave emitting source. These properties are measured via correlations between specific pairs of parameters. In this section, four such correlations are investigated.

7.1 q-$\mathcal{M}_c$ relation

The GWTC-1 contains a total of 11 individual events. Six of these events (GW150914, GW151012, GW151226, GW170104, GW170608, GW170823) were recorded exclusively by the Hanford (H1) and Livingston (L1) Advanced LIGO interferometers, whereas the other five (GW170729, GW170809, GW170814, GW170817, GW170818) were detected by all three H1, L1 and VIRGO interferometers. However, three of these events (GW151226, GW170608 and GW170729) had convergence errors when put through the PyCBC Inference toolkit and event GW170817[46] is classified as a BNS (binary neutron star) event with very different properties to BBH events. These four events will therefore be omitted in the following treatments.

When studying data from gravitational wave sources, it is sometimes useful to introduce new parameters to better describe the framework in which we are working. In terms of mass, one may chose to work in terms of the primary and secondary mass, but this is not unique. Two other important quantities allow to describe compact binary sources, the *chirp mass* and the *mass ratio*[47]. The former is description of the leading-order orbital evolution of the BBH that results from the energy loss due to gravitational radiation. It is given by:

$$\mathcal{M}_c = \frac{(M_1 M_2)^{3/5}}{(M_1 + M_2)^{1/5}} \tag{64}$$

where M_1 is the primary mass, M_2 is the secondary mass, $\mu = M_1 M_2/(M_1 + M_2)$ is the reduced mass and $M = M_1 + M_2$ is the total mass of the binary. One may also describe this quantity in terms of the mass ratio:

$$\mathcal{M}_c = \left[\frac{q}{(1+q)^2}\right]^{3/5} M \tag{65}$$

where q is defined as:

$$q = \frac{M_2}{M_1}, \tag{66}$$

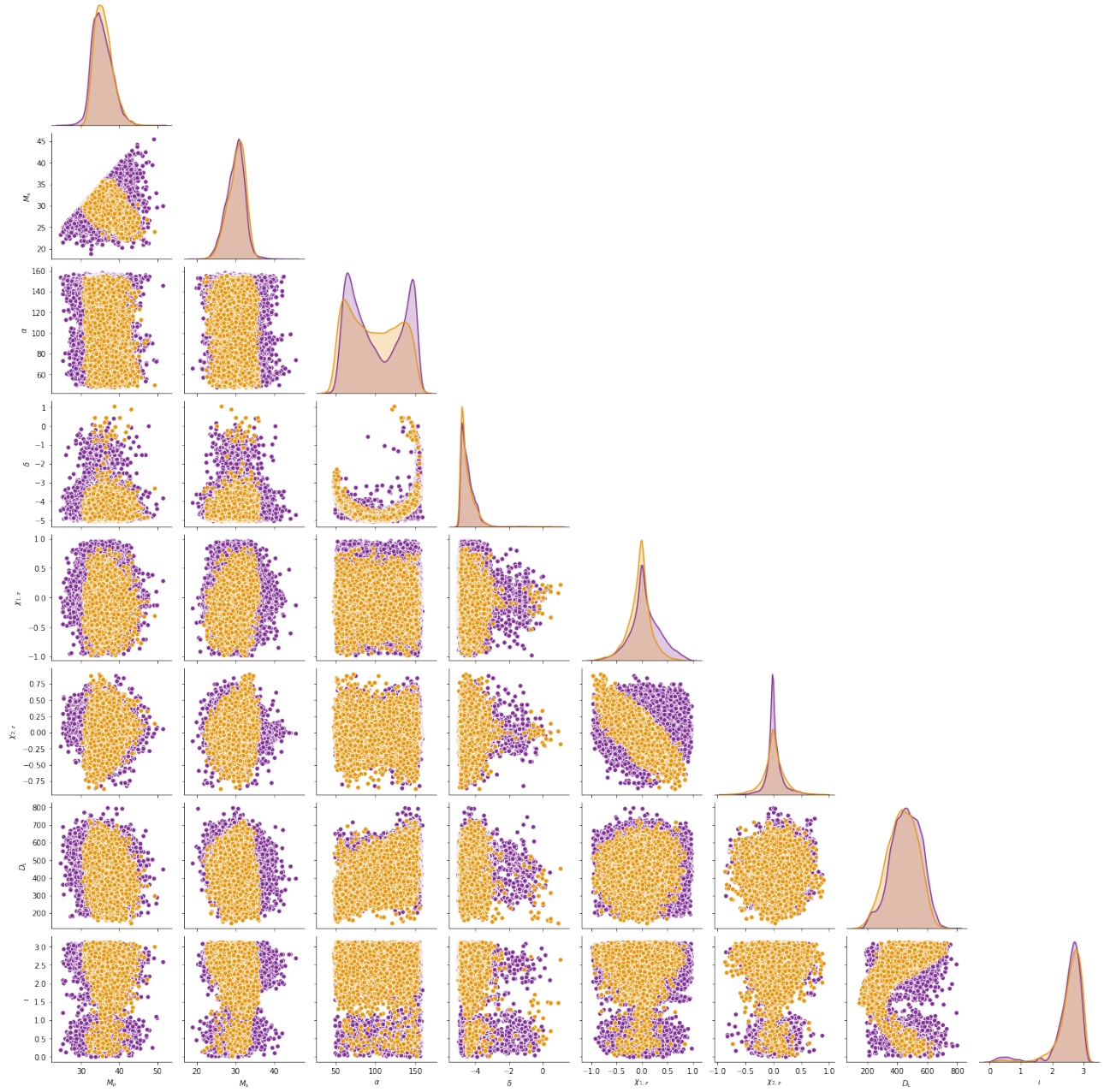

Figure 8: Posterior distributions of sampling parameters obtained from the strain data of event GW150914. The results from the PyCBC inference sampler using the dynesty sampling method are colored purple, whereas the samples obtained from the public database (GWTC-1) are colored yellow.

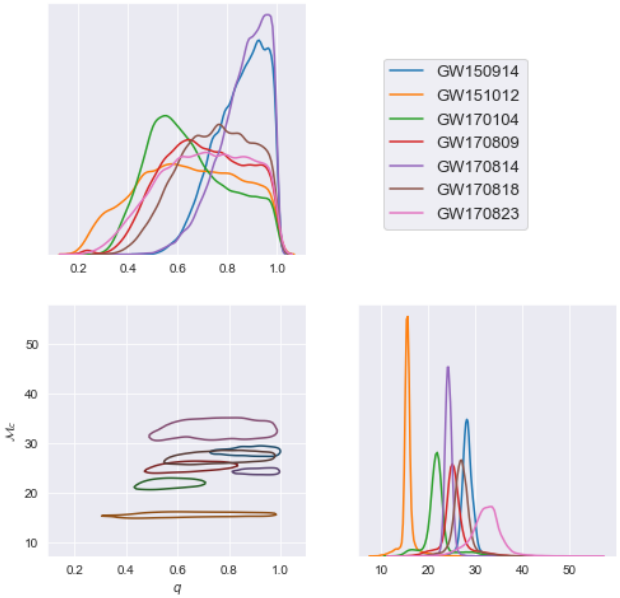

Figure 9: Distribution of the samples in the mass ratio-chirp mass space. The contours represent the 50% confidence intervals, and the marginalised posteriors are plotted on the diagonal.

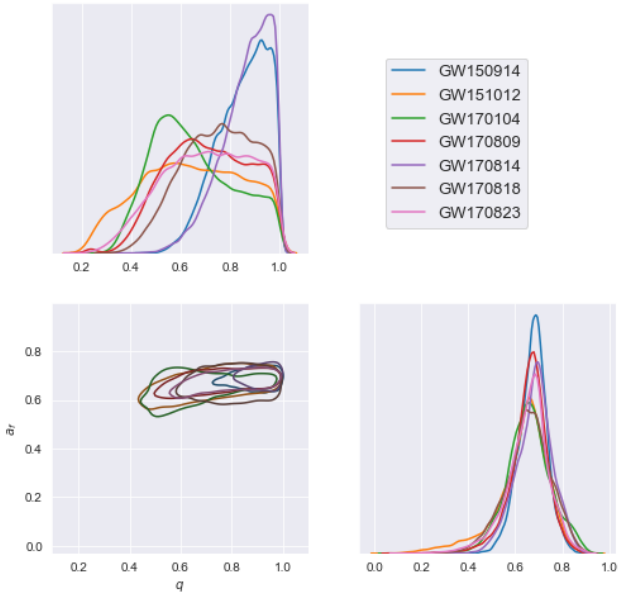

Figure 10: Distribution of the samples in the mass ratio-final spin space. The contours represent the 50% confidence intervals, and the marginalised posteriors are plotted on the diagonal.

such that it is bounded between 0 and 1. This is a crucial parameter in the analysis of EMRIs and binary systems with a large disparity in component masses.

Figure 9 compares these two quantities for the events contained within the GWTC-1. We note that the mass ratio of the sampled events are distributed closer to 1, indicating a preference for binaries with relatively similar component masses. However, the fairly wide distribution of chirp masses, from about $15M_\odot$ to about $35M_\odot$ indicates that the total mass of the system may well vary greatly from one event to the next, obviously always limited by the detection capabilities of the Advanced LIGO/VIRGO telescopes ($10 - 80M_\odot$).

7.2 q-a_f relation

Apart from mass parameter correlations, one may also be interested to investigate the relation in the mass-spin coupling regime, by studying correlations of mass parameters with spin parameters. One such relation involves looking at the mass ratio and the final spin of the remnant left after the merger, given by the the dimensionless parameter a_f, which also takes values from 0 to 1.

Figure 10 illustrates a clear skew to high values of both mass ratio and remnant spin for all events sampled. The latter can be explained by considering that the final spin of the remnant has contributions not only from the spins of the individual components of the binary (which may be zero or not) but also from the orbital angular momentum at the innermost stable circular orbit. Therefore, we expect by default that the remnant will have some amount of spin due exclusively to the compact binary, which will be subject to additional gains from each individual parent.

7.3 q-χ_{eff} relation

Another useful spin parameter used in the analysis of gravitational wave signals from compact binaries is the *effective spin*, χ_{eff}, which is a projection of the spin of the component that describes the leading order evolution of the binary[48]. It is given by the mass-weighted average of the component spins ($\chi_{1,2}$):

$$\chi_{eff} = \frac{(m_1\chi_1 + m_2\chi_2)}{m_1 + m_2} \tag{67}$$

Similar to the relation above, Figure 11 clearly shows a preferred area that the samples inhabit. In this case, however, we find that the values of χ_{eff} are centred around zero. This may hint at the existence of sources of spin suppression of the remnant black hole coming directly from the component spins[48].

7.4 a_f-χ_{eff} relation

In order to piece together the spin analysis of the sampled compact binaries, and thus conclude our comparative analysis of BBH sample properties, it is useful

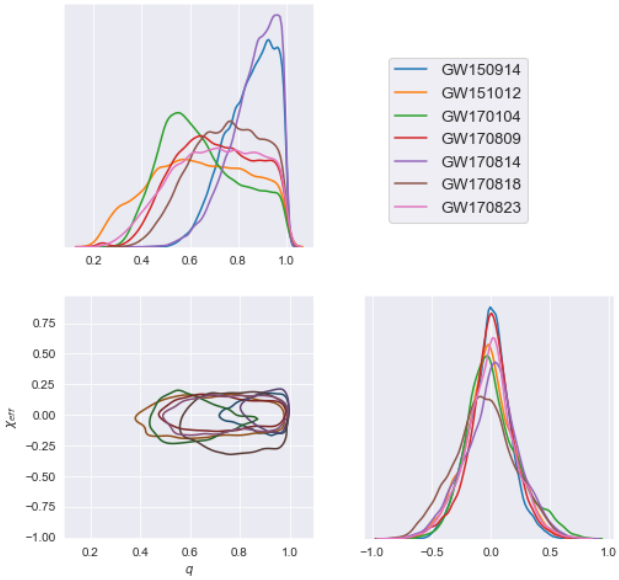

Figure 11: Distribution of the samples in the mass ratio-effective spin space. The contours represent the 50% confidence intervals, and the marginalised posteriors are plotted on the diagonal.

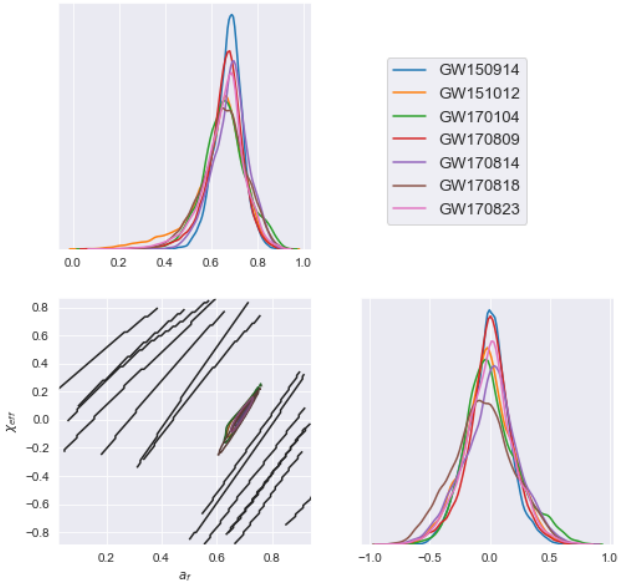

Figure 12: Distribution of the samples in the final spin-effective spin space. The contours represent the 50% confidence intervals, and the marginalised posteriors are plotted on the diagonal.

to make an analysis of the relationship between the effective spin of the inspiral and the final spin of the remnant.

Figure 12, showcases a very interesting result in terms of their dependence. Whereas correlations were not obvious in previous comparisons, the χ_{eff} and a_f parameters exhibit a clear proportionality relation. In order to explain this correlation from an astrophysical point of view, we set ourselves at $\chi_{eff} = 0$. This value can only be obtained in two distinct situations. The first scenario is a binary system of mass ratio $q \sim 1$ with perfectly anti-aligned components. The second, and probably more interesting in terms of physical consequences, requires that the binary system be formed of perfectly non-rotating, Schwarzschild black holes. In this case, one would find a vanishing effective spin due to the explicit component-spin-dependency that can be seen in Equation 67. Under the current paradigm of black hole formation due to the collapse of a star (which we will revisit in the following sections), violent phenomena associated with supernovae and gravitational collapse would most likely not be perfectly spherically symmetric, thus making it virtually impossible for a remnant such as a BH to have no spin. Therefore, if the scenario of the Schwarzschild BBH is to be responsible for these vanishing values of χ_{eff}, one might need to reconsider the nature of the component black holes at hand.

Primordial black holes (PBHs) are intriguing yet very promising candidates in both their formation channel and properties. They are formed due to large perturbations in the cosmological curvature power spectrum after inflation collapsing during the radiation-dominated era. Individually, these objects form with zero spin values and can have masses in the detectable range of Advanced LIGO/VIRGO telescopes.[49] Their availability during the early stages of the Universe allows them to form clusters with binaries that merge well within the age of the Universe. Hierarchical merging within these clusters allows PBHs to grow in mass as well as pick up some residual spin directly from the orbital angular momentum of the binary orbit. Studies have already proposed the possibility that these objects have a high degree of contribution to the gravitational spectrum, including events with binaries similar to those showcased in the figures above.[50]

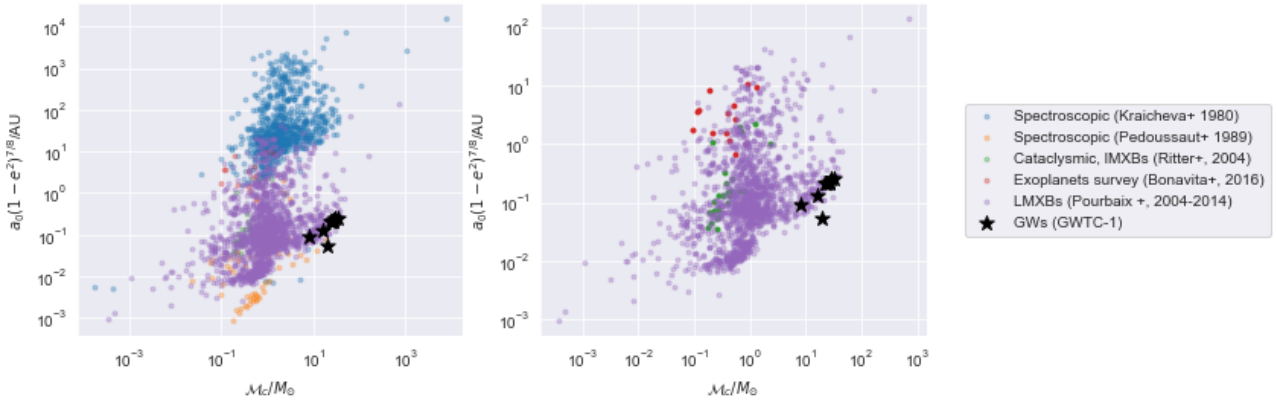

Figure 13: Distribution of the eccentricity-corrected initial separation of stellar binaries and BBHs with respect to their chirp mass. Stellar binaries are colored whereas gravitational-wave emitting sources are plotted as black stars.

8 Comparative analysis of GWTC-1 binaries with stellar binaries

The current, most accepted paradigm of gravitational-wave emitting BBH formation and evolution establishes that these systems would be the remnants of a stellar binary whose components evolved in parallel and where at least one star (in the case of binaries with one black hole and one companion star) collapsed into a BH. We have seen, however, several instances where this line of thought may be challenged by properties of the remnant black hole, one such being the values obtained for the effective spin of the system (see Section 7.3). These suggest that the components may have no spin in the inspiral phase and that the spin of the remnant may be fully due to the orbital angular momentum at the ISCO.

If the stellar binary paradigm is correct we can expect that, assuming kickback effects from supernovae and other violent phenomena do not disturb the orbit significantly, and early inspiral BBH will somewhat mirror the properties of its parent system. On top of that, there are many different types of stellar binaries, thus posing the question of which ones satisfy the conditions necessary to evolve into BBHs detectable by the Advanced LIGO/VIRGO band.

In this Section, we present a study that would have the orbital properties of GWTC-1 inspirals compared directly with stellar binaries from catalogues extracted from the VizieR database. We are looking at identifying the type of stellar binary whose orbital properties will most closely follow the behaviour BBH inspiral if any and whether correlations hold for both.

The "initial" separation (the separation at which point the binary enters the detectable frequency range of the Advanced LIGO/VIRGO detectors), as far as BBHs are concerned, is a crucial parameter in studying the behavioural patterns of the system at hand. In its derivation from the quadrupole approximation, it is explicitly dependant on the coalescence time, which is required to be within the age of the Universe. By integrating Equation 33 within the bounds of the age of the Universe, we obtain that:

$$a_0 = 1.6\ R_\odot \left(\frac{M_1}{M_\odot}\right)^{3/4} \left[q(1+q)F(e)\left(\frac{t_{coal}}{1\text{Gyr}}\right)\right]^{1/4} \tag{68}$$

where the factor $F(e)$, see Equation 31, corrects for the eccentricity. PyCBC Inference cannot sample for the eccentricity of BBHs; however, all orbits of these systems tend to circularise, and studies made on massive black hole binaries and at the centre of AGN accretion disks find that circularisation timescales are extremely fast compared to the entire coalescence timescale (of a few Myrs)[3, 51], or that the orbit may be considered circular by the time the components are separated by $a_0 \leq 10^{-3}$ AU[52]. In general, the main assumption is that, by the time BBHs enter the detectable band of Advanced LIGO/VIRGO, their eccentricity will have significantly decreased if not become fully circular and thus we pick and eccentricity across the board of $e = 0.1$, to allow for a margin of tolerance. Additionally, as we have said before, we require that the coalescence time be, at maximum, of the age of the Universe ($t_{coal} = 14$Gyr). Substituting parameters plus the appropriate numerical values from the sampling into Equation 68, one can plot the distribution of binary systems in this space with respect to the chirp mass of the system. This is a good parameter to investigate since it defines the leading order evolution of the binary, and is a widely used variable when describing the size (mass) of the system at hand.

The stellar binaries being investigated are extracted directly from the VizieR database[53]; a short description of each is provided below.

Pédoussaut *et. al.*[54] published, between 1982 and 1986, a compendium of 436 orbits of spectroscopic binaries recorded by the "Observatoire de Toulouse". The catalogue provides, among others, the corresponding identifying parameters of each system (HD, BH and name), the sky localisation, magnitudes, spectral types and orbital properties (period and semimajor axis corrected for the binary inclination) which are those of interest to us.

Kraicheva *et. al.*[55] also published (this time in 1980) a collection of the 7th Catalogue of Spectroscopic Binary Stars (Batten, 1979) together with its 11th, 12th and 13th Supplements provided by Pédoussaut *et. al.* It improves these catalogues by computing additional parameters such as the masses of components, mass ratios, semiaxes or orbits, orbital angular momenta and specific orbital momenta.

Bonavita *et. al*[56] published in 2016 the results of the SPOTS (Search for Planets Orbiting Two Stars) survey, an ongoing study of exoplanets orbiting close binaries in 24 direct imaging surveys. The total sample includes 117 tight systems and uses Monte Carlo and Bayesian methods to infer expected values of their properties. It provides information on distances to the sources, stellar masses amd ratios and separations of the critical semimajor axis for dynamical stability, amongst others.

Ritter and Kolb[57] published in 2003 a catalogue of 656 binary orbits among which 472 correspond to cataclysmic binaries, 71 correspond to low-mass X-ray binaries and 113 are attributed to related objects with known or inferred orbital periods. The catalogue contains sky coordinates, apparent magnitudes, orbital parameters (such as the period, semimajor axis and eccentricity) and stellar parameters (mass, mass ratios and others).

Finally, Pourbaix *et. al.*[58] published in 2004 the Ninth Catalogue of Spectroscopic Binary Orbits, which provides a compilation of 2386 spectroscopic binary orbits from surveys performed over a 35-year period by Batten and collaborators. Among others, the catalogue includes orbital properties such as period, eccentricity and radial velocities, which are used to calculate the mass ratio of the components.

Figure 13 showcases the population of stellar binaries an BBHs in the separation-mass space. Additionally, the initial separation includes an explicitly eccentricity-dependant term that acts as a correction between binaries. Although widely distributed in terms of their initial separations, the systems occupy a fairly narrow band in terms of chirp mass. However, stellar systems populate a range of chirp masses that are, on average, under that of the GWTC-1 events. This is problematic to the black hole formation via stellar collapse model, since we expect some mass to be expelled during supernovae. This conundrum could be resolved either by introducing other external mechanisms that would supply the black holes with additional mass, such as the formation of accretion disks. The main issue with this mechanism is that the disks of matter around the black hole will inevitably induce some spin onto it, thus going back to the issue of the apparent vanishing of spin projection in black holes seen in the effective chi parameter. Alternatively, one can consider the possibility that other candidates are available to replace these binary companions, which better fit our requirements. One such candidate, which has been mentioned before were primordial black holes. Since these objects form as the result of cosmological phenomena rather than stellar, it would be possible to find object in the mass range of the GWTC-1 events that do not necessarily follow patterns directly related to those of stellar binaries.

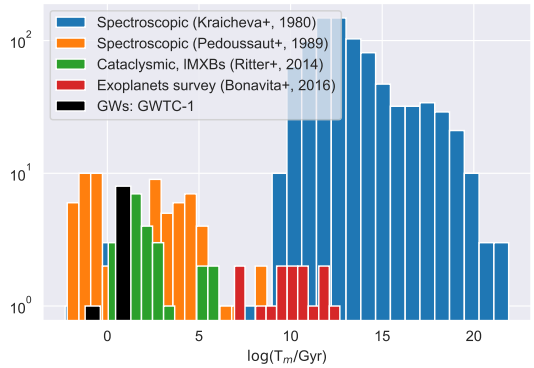

Figure 14: Logarithmic distribution of merger times for stellar and black hole binaries.

This necessarily raises another question: in the eventuality that stellar binaries are indeed responsible for the formation of GWTC-1 BBHs, is it possible for their own orbital decay to be slow enough so that the stars will be able to collapse (assuming negligible kickback effects) and form a gravitational-wave emitting binary? The merger time of a binary is given to us by the following formula[11]:

$$T_m = 3.81 \text{ Gyr} \left(\frac{a_0}{10^{-2}\text{AU}}\right)^4 \frac{\left(1-e_0^2\right)^{7/2} M_\odot^3}{M_1 M_2 \left(M_1+M_2\right)} \quad (69)$$

which we can compute for both the BBHs and the stellar binaries.

Figure 14 proposes that the merger time of the GWTC-1 binaries would indeed be within the range

of stellar binary populations that also fulfil separation requirements as presented in Figure 13. Others, such as the spectroscopic binary population, seem to be off in both the merger time required and the separation requirements. This information is indeed rather helpful, as we can start to observe some types of binaries accommodate better the conditions to form stable binary black hole orbits that will, at some point, enter the Advanced LIGO/VIRGO detectable frequency band.

It is clear that the problem becomes increasingly complex the more we delve into it, with indications that the standard line of thought as far as BBH formation is concerned may not be exactly right, but with other data that seems to fit.

9 Conclusions

The field of gravitational wave astronomy may well be entering a new golden age as more detectors are introduced into the Advanced LIGO/VIRGO network (KAGRA[41], LIGO India[42] and the Einstein Telescope[43]) and larger repositories of data are becoming available for research. Although this project was solely focused on data analysis within the detectability capabilities of land-based interferometers, it is worth noting that the addition of other observatories designed to detect gravitational radiation outside of the Advanced LIGO/VIRGO band will also come with crucial consequences both in our understanding of gravitational-wave emitting sources and future prospects in the field.

In the early sections of this project, we provided insight into parameter extraction techniques using the PyCBC Inference toolkit, including how the input is constructed and the details of how bayesian inference models were added to extract the posterior density distribution for each sampling parameter.

A comparative analysis of the samples was then performed, which allows to draw conclusions on the physical properties and behaviours of BBHs, both at the inspiral and post-merger phases. In this section, indications that could challenge the current, most accepted model of BBH formation and evolution via the collapse of stellar components in a stellar binary, became apparent. Average values of zero of the effective spin of the orbit for all events analysed suggest peculiar spin configurations from the binary components, which can only be explained via perfectly anti-aligned component spins with equal masses or by considering alternative spinless binary companions. Further research into the formation rate of perfectly anti-aligned binary black holes systems from a stellar binary is necessary in order to be conclusive about this result. However, candidates such as primordial black holes (which have no spin) would viably explain this phenomenon[59].

To address the challenges to the stellar binary model of BBH formation, a comparative analysis of orbital and physical properties of GWTC-1 inspirals and stellar binaries was introduced. The main assumption was that if kickback effects due to supernovae and other violent phenomena in stellar binaries were not strong enough to fully destabilise the orbit, then one would expect to observe similar properties in their orbits and those of GWTC-1 events, at least in the early inspiral. The results show that, solely based on the initial separation of the binary components, a population of stellar binaries could indeed evolve into a binary system of relativistic components that would create a gravitational-wave emitting compact binary. However, results also showcase an apparent deficit of mass that would be required to form BBHs with the chirp mass obtained from the GWTC-1 catalogue.

As the amount of data available to the public increases[60], so will our understanding of gravitational-wave emitting sources. There are already clear indications in the available data that there are still many unknowns in the properties of compact binaries, including their precise nature. Future runs of the Advanced LIGO/VIRGO interferometers is expected to provide a large number of diverse systems to analyse. Furthermore, when detectors like LISA[39], SKA[40] or the Einstein Telescope[43] become operative, we will have access to a very wide range of GW frequencies, emitted by a variety of source types. In this project, we propose that other candidates are already available in theory. Primordial black holes, among these, are promising in their relatively similar behaviour to stellar black holes at the astrophysical level. Additionally, studies show that, in the absence of any additional accretion processes, they would be able to reach masses within the detectable range of Advanced LIGO/VIRGO interferometers; their spinless nature would also provide an answer to some conundra in the data, and would allow for the possibility of moderately spinning components via hierarchical merging[61]. Nevertheless, the results of this project remain largely inconclusive until more events are available and thus a larger statistical sample of data. This project serves rather to propose an inquiry into the specific questions raised once more data can be used.

Acknowledgements

The author of this project would like to thank Professor García-Bellido for his continuous support and input throughout the duration of the project, which allowed it to go forward, and who encouraged me to always push the research further, as well as the In-

stituto de Física Teórica (IFT) and the Universidad Autónoma de Madrid (UAM).

This research has made use of data, software and/or web tools obtained from the Gravitational Wave Open Science Center (`https://www.gw-openscience.org`), a service of LIGO Laboratory, the LIGO Scientific Collaboration and the Virgo Collaboration. LIGO is funded by the U.S. National Science Foundation. Virgo is funded by the French Centre National de Recherche Scientifique (CNRS), the Italian Istituto Nazionale della Fisica Nucleare (INFN) and the Dutch Nikhef, with contributions by Polish and Hungarian institutes.

This research has made use of the VizieR catalogue access tool, CDS, Strasbourg, France (DOI: 10.26093/cds/vizier). The original description of the VizieR service was published in 2000, A&AS 143, 23.

References

[1] Albert Einstein. "Über Gravitationswellen". In: *Sitzungsber. Preuss. Akad. Wiss. Berlin (Math. Phys.)* 1918 (1918), pp. 154–167.

[2] B. P. Abbott et al. "Observation of Gravitational Waves from a Binary Black Hole Merger". In: *Phys. Rev. Lett.* 116 (6 Feb. 2016), p. 061102. DOI: 10.1103/PhysRevLett.116.061102. URL: https://link.aps.org/doi/10.1103/PhysRevLett.116.061102.

[3] M. Maggiore. *Gravitational Waves: Volume 1: Theory and Experiments*. Gravitational Waves. OUP Oxford, 2008. ISBN: 9780198570745. URL: https://books.google.es/books?id=AqVpQgAACAAJ.

[4] J. Stewart and J.M. Stewart. *Advanced General Relativity*. Cambridge Monographs on Mathematical Physics. Cambridge University Press, 1993. ISBN: 9780521449465. URL: https://books.google.es/books?id=LZrjJ2P1J1sC.

[5] R. A. Hulse and J. H. Taylor. "Discovery of a pulsar in a binary system." In: 195 (Jan. 1975), pp. L51–L53. DOI: 10.1086/181708.

[6] B. P. Abbott et al. "GW170814: A Three-Detector Observation of Gravitational Waves from a Binary Black Hole Coalescence". In: 119.14, 141101 (Oct. 2017), p. 141101. DOI: 10.1103/PhysRevLett.119.141101. arXiv: 1709.09660 [gr-qc].

[7] J. A. Wheeler. "Superdense Stars." In: *Annual Review of Astronomy and Astrophysics* 4.1 (1966), pp. 393–432. DOI: 10.1146/annurev.aa.04.090166.002141.

[8] A. A. Starobinskiĭ. "Spectrum of relict gravitational radiation and the early state of the universe". In: *Soviet Journal of Experimental and Theoretical Physics Letters* 30 (Dec. 1979), p. 682.

[9] R. Sturani et al. "Complete phenomenological gravitational waveforms from spinning coalescing binaries". In: *Journal of Physics Conference Series*. Vol. 243. Journal of Physics Conference Series. Aug. 2010, p. 012007. DOI: 10.1088/1742-6596/243/1/012007. arXiv: 1005.0551 [gr-qc].

[10] B. P. Abbott et al. "The basic physics of the binary black hole merger GW150914". In: *Annalen der Physik* 529.1-2 (Jan. 2017), p. 1600209. DOI: 10.1002/andp.201600209. arXiv: 1608.01940 [gr-qc].

[11] P. C. Peters. "Gravitational Radiation and the Motion of Two Point Masses". In: *Phys. Rev.* 136 (4B Nov. 1964), B1224–B1232. DOI: 10.1103/PhysRev.136.B1224. URL: https://link.aps.org/doi/10.1103/PhysRev.136.B1224.

[12] Marco Celoria et al. "Lecture notes on black hole binary astrophysics". In: *arXiv e-prints*, arXiv:1807.11489 (July 2018), arXiv:1807.11489. arXiv: 1807.11489 [astro-ph.GA].

[13] A. Buonanno and T. Damour. "Effective one-body approach to general relativistic two-body dynamics". In: 59.8, 084006 (Apr. 1999), p. 084006. DOI: 10.1103/PhysRevD.59.084006. arXiv: gr-qc/9811091 [gr-qc].

[14] C.W. Misner et al. *Gravitation*. Princeton University Press, 2017. ISBN: 9781400889099. URL: https://books.google.es/books?id=zAAuDwAAQBAJ.

[15] Luis Lehner. "TOPICAL REVIEW: Numerical relativity: a review". In: *Classical and Quantum Gravity* 18.17 (Sept. 2001), R25–R86. DOI: 10.1088/0264-9381/18/17/202. arXiv: gr-qc/0106072 [gr-qc].

[16] Leor Barack et al. "Black holes, gravitational waves and fundamental physics: a roadmap". In: *Classical and Quantum Gravity* 36.14, 143001 (July 2019), p. 143001. DOI: 10.1088/1361-6382/ab0587. arXiv: 1806.05195 [gr-qc].

[17] Emanuele Berti, Vitor Cardoso, and Clifford M. Will. "Gravitational-wave spectroscopy of massive black holes with the space interferometer LISA". In: 73.6, 064030 (Mar. 2006), p. 064030. DOI: 10.1103/PhysRevD.73.064030. arXiv: gr-qc/0512160 [gr-qc].

[18] LIGO Scientific Collaboration et al. "Advanced LIGO". In: *Classical and Quantum Gravity* 32.7, 074001 (Apr. 2015), p. 074001. DOI: 10.1088/0264-9381/32/7/074001. arXiv: 1411.4547 [gr-qc].

[19] Albert A. Michelson and Edward W. Morley. "On the Relative Motion of the Earth and of the Luminiferous Ether". In: *Sidereal Messenger* 6 (Nov. 1887), pp. 306–310.

[20] B. P. Abbott et al. "GW150914: The Advanced LIGO Detectors in the Era of First Discoveries". In: 116.13, 131103 (Apr. 2016), p. 131103. DOI: 10.1103/PhysRevLett.116.131103. arXiv: 1602.03838 [gr-qc].

[21] David G. Blair. *The Detection of Gravitational Waves*. 2005.

[22] Alessandra Buonanno and Yanbei Chen. "Signal recycled laser-interferometer gravitational-wave detectors as optical springs". In: 65.4, 042001 (Feb. 2002), p. 042001. DOI: 10.1103/PhysRevD.65.042001. arXiv: gr-qc/0107021 [gr-qc].

[23] Tobin T. Fricke et al. "DC readout experiment in Enhanced LIGO". In: *Classical and Quantum Gravity* 29.6, 065005 (Mar. 2012), p. 065005. DOI: 10.1088/0264-9381/29/6/065005. arXiv: 1110.2815 [physics.ins-det].

[24] D. V. Martynov et al. "Sensitivity of the Advanced LIGO detectors at the beginning of gravitational wave astronomy". In: 93.11, 112004 (June 2016), p. 112004. DOI: 10.1103/PhysRevD.93.112004. arXiv: 1604.00439 [astro-ph.IM].

[25] G. Turin. "An introduction to matched filters". In: *IRE Transactions on Information Theory* 6.3 (1960), pp. 311–329.

[26] Carl W. Helstrom. "IV - Detection of a Known Signal". In: *Statistical Theory of Signal Detection (2nd Edition)*. Ed. by Carl W. Helstrom. 2nd Edition. International Series of Monographs in Electronics and Instrumentation. Pergamon, 1968, pp. 102–147. ISBN: 978-0-08-013265-5. DOI: https://doi.org/10.1016/B978-0-08-013265-5.50010-0.

[27] Benjamin J. Owen and B. S. Sathyaprakash. "Matched filtering of gravitational waves from inspiraling compact binaries: Computational cost and template placement". In: 60.2, 022002 (July 1999), p. 022002. DOI: 10.1103/PhysRevD.60.022002. arXiv: gr-qc/9808076 [gr-qc].

[28] B. P. Abbott et al. "GW150914: First results from the search for binary black hole coalescence with Advanced LIGO". In: 93.12, 122003 (June 2016), p. 122003. DOI: 10.1103/PhysRevD.93.122003. arXiv: 1602.03839 [gr-qc].

[29] Samantha A. Usman et al. "The PyCBC search for gravitational waves from compact binary coalescence". In: *Classical and Quantum Gravity* 33.21, 215004 (Nov. 2016), p. 215004. DOI: 10.1088/0264-9381/33/21/215004. arXiv: 1508.02357 [gr-qc].

[30] Neil J. Cornish and Tyson B. Littenberg. "Bayeswave: Bayesian inference for gravitational wave bursts and instrument glitches". In: *Classical and Quantum Gravity* 32.13, 135012 (July 2015), p. 135012. DOI: 10.1088/0264-9381/32/13/135012. arXiv: 1410.3835 [gr-qc].

[31] Ben Farr et al. "Parameter Estimation on Gravitational Waves from Neutron-star Binaries with Spinning Components". In: 825.2, 116 (July 2016), p. 116. DOI: 10.3847/0004-637X/825/2/116. arXiv: 1508.05336 [astro-ph.HE].

[32] Joshua S. Speagle. "DYNESTY: a dynamic nested sampling package for estimating Bayesian posteriors and evidences". In: 493.3 (Apr. 2020), pp. 3132–3158. DOI: 10.1093/mnras/staa278. arXiv: 1904.02180 [astro-ph.IM].

[33] Edward Higson et al. "Dynamic nested sampling: an improved algorithm for parameter estimation and evidence calculation". In: *Statistics and Computing* 29.5 (Sept. 2019), pp. 891–913. DOI: 10.1007/s11222-018-9844-0. arXiv: 1704.03459 [stat.CO].

[34] The LIGO Scientific Collaboration et al. "Open data from the first and second observing runs of Advanced LIGO and Advanced Virgo". In: *arXiv e-prints*, arXiv:1912.11716 (Dec. 2019), arXiv:1912.11716. arXiv: 1912.11716 [gr-qc].

[35] M. G. Haehnelt. "Low-Frequency Gravitational Waves from Supermassive Black-Holes". In: 269 (July 1994), p. 199. DOI: 10.1093/mnras/269.1.199. arXiv: astro-ph/9405032 [astro-ph].

[36] Andy D. Goulding et al. "Discovery of a Close-separation Binary Quasar at the Heart of a z 0.2 Merging Galaxy and Its Implications for Low-frequency Gravitational Waves". In: 879.2, L21 (July 2019), p. L21. DOI: 10.3847/2041-8213/ab2a14. arXiv: 1907.03757 [astro-ph.GA].

[37] Christopher Berry et al. "The unique potential of extreme mass-ratio inspirals for gravitational-wave astronomy". In: 51.3, 42 (May 2019), p. 42. arXiv: 1903.03686 [astro-ph.HE].

[38] Matteo Bonetti and Alberto Sesana. "Gravitational wave background from extreme mass ratio inspirals". In: *arXiv e-prints*, arXiv:2007.14403 (July 2020), arXiv:2007.14403. arXiv: 2007.14403 [astro-ph.GA].

[39] Enrico Barausse et al. "Prospects for Fundamental Physics with LISA". In: *arXiv e-prints*, arXiv:2001.09793 (Jan. 2020), arXiv:2001.09793. arXiv: 2001.09793 [gr-qc].

[40] A. Weltman et al. "Fundamental physics with the Square Kilometre Array". In: 37, e002 (Jan. 2020), e002. DOI: 10.1017/pasa.2019.42. arXiv: 1810.02680 [astro-ph.CO].

[41] Kagra Collaboration et al. "KAGRA: 2.5 generation interferometric gravitational wave detector". In: *Nature Astronomy* 3 (Jan. 2019), pp. 35–40. DOI: 10.1038/s41550-018-0658-y. arXiv: 1811.08079 [gr-qc].

[42] C. S. Unnikrishnan. "IndIGO and Ligo-India Scope and Plans for Gravitational Wave Research and Precision Metrology in India". In: *International Journal of Modern Physics D* 22.1, 1341010 (Jan. 2013), p. 1341010. DOI: 10.1142/S0218271813410101. arXiv: 1510.06059 [physics.ins-det].

[43] Michele Maggiore et al. "Science case for the Einstein telescope". In: 2020.3, 050 (Mar. 2020), p. 050. DOI: 10.1088/1475-7516/2020/03/050. arXiv: 1912.02622 [astro-ph.CO].

[44] B. P. Abbott et al. "GWTC-1: A Gravitational-Wave Transient Catalog of Compact Binary Mergers Observed by LIGO and Virgo during the First and Second Observing Runs". In: *Physical Review X* 9.3, 031040 (July 2019), p. 031040. DOI: 10.1103/PhysRevX.9.031040. arXiv: 1811.12907 [astro-ph.HE].

[45] LIGO Scientific Collaboration and Virgo Collaboration. *Parameter estimation sample release for GWTC-1*. Tech. rep. 2020. DOI: 10.7935/KSX7-QQ51. URL: https://dcc.ligo.org/LIGO-P1800370/public.

[46] B. P. Abbott et al. "GW170817: Observation of Gravitational Waves from a Binary Neutron Star Inspiral". In: 119.16, 161101 (Oct. 2017), p. 161101. DOI: 10.1103/PhysRevLett.119.161101. arXiv: 1710.05832 [gr-qc].

[47] Curt Cutler and Éanna E. Flanagan. "Gravitational waves from merging compact binaries: How accurately can one extract the binary's parameters from the inspiral waveform\?" In: 49.6 (Mar. 1994), pp. 2658–2697. DOI: 10.1103/PhysRevD.49.2658. arXiv: gr-qc/9402014 [gr-qc].

[48] Simona Miller, Thomas A. Callister, and Will Farr. "The Low Effective Spin of Binary Black Holes and Implications for Individual Gravitational-Wave Events". In: *arXiv e-prints*, arXiv:2001.06051 (Jan. 2020), arXiv:2001.06051. arXiv: 2001.06051 [astro-ph.HE].

[49] Juan Garcıa-Bellido. "Massive Primordial Black Holes as Dark Matter and their detection with Gravitational Waves". In: *Journal of Physics Conference Series*. Vol. 840. Journal of Physics Conference Series. May 2017, p. 012032. DOI: 10.1088/1742-6596/840/1/012032. arXiv: 1702.08275 [astro-ph.CO].

[50] Andrew D. Gow et al. "Primordial black hole merger rates: distributions for multiple LIGO observables". In: 2020.1, 031 (Jan. 2020), p. 031. DOI: 10.1088/1475-7516/2020/01/031. arXiv: 1911.12685 [astro-ph.CO].

[51] Monica Colpi. "Massive Binary Black Holes in Galactic Nuclei and Their Path to Coalescence". In: 183.1-4 (Sept. 2014), pp. 189–221. DOI: 10.1007/s11214-014-0067-1. arXiv: 1407.3102 [astro-ph.GA].

[52] W. Ishibashi and M. Gröbner. "Evolution of binary black holes in AGN accretion discs: Disc-binary interaction and gravitational wave emission". In: 639, A108 (July 2020), A108. DOI: 10.1051/0004-6361/202037799. arXiv: 2006.07407 [astro-ph.GA].

[53] F. et. al Ochsenbein. *The VizieR database of astronomical catalogues*. DOI: 10.26093/cds/vizier.

[54] A. Pedoussaut et al. "Binaires spectroscopiques. 15e catalogue complemetaire." In: 75 (Nov. 1988), pp. 441–496.

[55] Z. Kraicheva et al. "Catalogue of physical parameters of spectroscopic binary stars." In: *Bulletin d'Information du Centre de Donnees Stellaires* 19 (July 1980), p. 71.

[56] M. Bonavita et al. "SPOTS: The Search for Planets Orbiting Two Stars. II. First constraints on the frequency of sub-stellar companions on wide circumbinary orbits". In: 593, A38 (Sept. 2016), A38. DOI: 10.1051/0004-6361/201628231. arXiv: 1605.03962 [astro-ph.EP].

[57] H. Ritter and U. Kolb. "Catalogue of cataclysmic binaries, low-mass X-ray binaries and related objects (Seventh edition)". In: 404 (June 2003), pp. 301–303. DOI: 10.1051/0004-6361:20030330. arXiv: astro-ph/0301444 [astro-ph].

[58] D. Pourbaix et al. "SB9: The ninth catalogue of spectroscopic binary orbits". In: 424 (Sept. 2004), pp. 727–732. DOI: 10.1051/0004-6361:20041213. arXiv: astro-ph/0406573 [astro-ph].

[59] Juan García-Bellido. "Primordial black holes and the origin of the matter–antimatter asymmetry". In: *Phil. Trans. Roy. Soc. Lond. A* 377.2161 (2019). Ed. by John Dainton, p. 20190091. DOI: 10.1098/rsta.2019.0091.

[60] B. P. Abbott et al. "Prospects for observing and localizing gravitational-wave transients with Advanced LIGO, Advanced Virgo and KAGRA". In: *Living Reviews in Relativity* 21.1, 3 (Apr. 2018), p. 3. DOI: 10.1007/s41114-018-0012-9. arXiv: 1304.0670 [gr-qc].

[61] V. De Luca et al. "Primordial black holes confront LIGO/Virgo data: current situation". In: 2020.6, 044 (June 2020), p. 044. DOI: 10.1088/1475-7516/2020/06/044. arXiv: 2005.05641 [astro-ph.CO].

A Tables of numerical values

Table 1: Statistical estimates of sampling parameters of GWTC-1 events obtained from dynamically nested sampling with PyCBC Inference.

PyCBC Inference								
Name	α (deg)	δ (h)	D_L (Mpc)	ι (rad)	M_1 ($M_\odot$)	M_2 ($M_\odot$)	$\chi_{1,z}$	$\chi_{2,z}$
GW150914	101.99±33.17	-4.45±0.46	460.71±97.89	2.52±0.51	34.08±3.43	31.46±3.56	-0.37±-0.03	-0.00±0.19
GW151012	212.72±82.09	-0.72±2.80	814.64±115.32	1.42±0.75	16.57±4.75	21.35±6.23	-0.35±-0.02	0.05±0.19
GW151226	-	-	-	-	-	-	-	-
GW170104	159.78±85.96	1.50±2.92	780.96±152.87	1.65±0.81	27.23±7.25	25.14±7.41	-0.45±-0.05	0.01±0.20
GW170608	-	-	-	-	-	-	-	-
GW170729	-	-	-	-	-	-	-	-
GW170809	15.48±3.95	-2.00±0.42	835.62±120.06	2.36±0.32	30.03±7.15	30.30±7.55	-0.36±-0.04	0.03±0.21
GW170814	46.55±1.59	-3.05±0.17	590.95±86.98	0.60±0.32	28.12±2.93	28.03±2.92	-0.49±-0.04	0.03±0.24
GW170817	-	-	-	-	-	-	-	-
GW170818	341.25±0.89	1.37±0.18	842.55±109.01	2.37±0.25	31.82±6.09	31.56±6.12	-0.53±-0.07	-0.15±0.23
GW170823	169.46±113.34	-0.68±2.38	858.55±115.22	1.58±0.50	37.25±8.89	38.97±9.29	-0.38±-0.02	0.02±0.22

Table 2: Statistical estimates of sampling parameters of GWTC-1 events obtained from the publicly available GWTC-1 catalog.

GWTC-1								
Name	α (deg)	δ (h)	D_L (Mpc)	ι (rad)	M_1 ($M_\odot$)	M_2 ($M_\odot$)	$\chi_{1,z}$	$\chi_{2,z}$
GW150914	97.79±30.68	-4.50±0.45	436.50±97.93	2.59±0.42	35.92±2.38	30.32±2.26	0.01±0.20	-0.04±0.20
GW151012	162.38±99.37	0.05±2.76	1089.99±321.42	1.63±1.00	24.88±6.49	13.50±2.76	0.07±0.21	0.04±0.22
GW151226	-	-	-	-	-	-	-	-
GW170104	147.99±70.34	2.12±2.45	989.06±268.16	1.48±0.94	31.15±4.02	20.12±2.93	-0.04±0.21	-0.05±0.22
GW170608	-	-	-	-	-	-	-	-
GW170729	17.73±7.49	-1.87±0.62	1014.35±214.95	2.53±0.33	35.39±4.44	23.89±3.19	-	-
GW170809	-	-	-	-	-	-	0.07±0.20	0.06±0.23
GW170814	46.03±3.12	-2.91±0.43	586.16±112.55	0.88±0.74	31.09±2.69	25.00±2.12	0.08±0.20	0.06±0.22
GW170817	-	-	-	-	-	-	-	-
GW170818	340.51±7.80	1.44±0.25	1068.37±248.84	2.43±0.32	35.87±3.82	26.53±2.95	-0.07±0.24	-0.09±0.24
GW170823	175.78±101.28	-0.09±2.69	1952.54±562.63	1.58±0.96	40.37±5.65	28.81±4.53	0.09±0.22	0.04±0.22